Please cite as:
Jones, T.J., McNamara, K., Eychenne, J., Rust, A.C., Cashman, K.V., Scheu, B. and Edwards, R., 2016. Primary and secondary fragmentation of crystal-bearing intermediate magma. *Journal of Volcanology and Geothermal Research*, *327*, pp.70-83.

Typeset manuscript available here:
https://doi.org/10.1016/j.jvolgeores.2016.06.022

Primary and secondary fragmentation of crystal-bearing intermediate magma

Thomas J. Jones[1,2*], Keri McNamara[2], Julia Eychenne[2], Alison C. Rust[2], Katharine V. Cashman[2], Bettina Scheu[3] and Robyn Edwards[2]

[1] Department of Earth Sciences, Durham University, Durham, DH1 3LE, UK

[2] School of Earth Sciences, University of Bristol, Wills Memorial Building, Bristol, BS8 1RJ, UK

[3] Department of Earth and Environmental Sciences, LMU Munich, Theresienstr. 41, 80333 Munich, Germany

Abstract

Crystal-rich intermediate magmas are subjected to both primary and secondary fragmentation processes, each of which may produce texturally distinct tephra. Of particular interest for volcanic hazards is the extent to which each process contributes ash to volcanic plumes. One way to address this question is by fragmenting pyroclasts under controlled conditions. We fragmented pumice samples from Soufriere Hills Volcano (SHV), Montserrat, by three methods: rapid decompression in a shock tube-like apparatus, impact by a falling piston, and milling in a ball mill. Grain size distributions of the products reveal that all three mechanisms produce fractal breakage patterns, and that the fractal dimension increases from a minimum of ~2.1 for decompression fragmentation (primary fragmentation) to a maximum of ~ 2.7 by repeated impact (secondary fragmentation). To assess the details of the fragmentation process, we quantified the shape, texture and components of constituent ash particles. Ash shape analysis shows that the axial ratio increases during milling and that particle convexity increases with repeated impacts. We also quantify the extent to which the matrix is separated from the crystals, which shows that secondary processes efficiently remove adhering matrix from crystals, particularly during milling (abrasion). Furthermore, measurements of crystal size distributions before (using x-ray computed tomography) and after (by componentry of individual grain size classes) decompression-driven fragmentation show not only that crystals influence particular size fractions across the total grain size distribution, but also that free crystals are smaller in the fragmented material than in the original pumice clast. Taken together, our results confirm previous work showing both the control of initial texture on the primary fragmentation process and the contributions of secondary processes to ash formation. Critically, however, our extension of previous analyses to characterization of shape, texture and componentry provides new analytical tools that can be used to assess contributions of secondary processes to ash deposits of uncertain or mixed origin. We illustrate this application with examples from SHV deposits.

Keywords: Volcanic ash; Fragmentation; Broken crystals; Milling; Fractals; X-ray computed tomography

1. Introduction

Volcanic ash is an inevitable product of nearly all explosive eruptions. Formed by fragmenting magma and/or rock, it is a particularly important hazard in the modern day, presenting a risk to aviation as well as to human health. Additionally, the associated risk is not confined to areas proximal to the volcano, but, as demonstrated by recent eruptions in Iceland and Chile, can also have far reaching impacts (e.g., Alfano et al., 2011). Understanding the origin of volcanic ash particles is thus critical for predicting the nature and extent of ash hazards. Volcanic ash can form by both primary and secondary processes; the former from volatile-driven decompression during magmatic ascent and the latter from post-fragmentation processes such as collisions within the conduit and transport in pyroclastic density currents (PDCs). Distinguishing between the products of primary and secondary fragmentation is necessary for a comprehensive understanding of volcanic ash deposits.

Primary magmatic fragmentation occurs either through ascent-driven vesiculation and expansion of a volatile phase or by rapid decompression, such as occurs because of edifice collapse. Typical fragmentation studies relate tephra characteristics (e.g., grain size distributions, GSDs) to the energy of the primary fragmentation (e.g. Walker, 1973). Secondary fragmentation further decreases the average grain size of a pyroclastic deposit. In PDCs, secondary ash-forming processes include both impact and abrasion (e.g. Freundt and Schmincke, 1992), which cause fining of vent-derived particles with increased transport distance (Dufek and Manga, 2008; Kueppers et al., 2012). The total grain size distribution (TGSD) produced by primary and secondary fragmentation processes, in turn, affects the efficiency of heat transfer (e.g., Zimanowski et al., 2003), PDC mobility (Félix and Thomas, 2004) and formation of co-PDC plumes (Eychenne et al., 2012). For this reason, identifying the contributions of co-PDC ash to the total deposit is particularly important for modelling ash plumes, especially in large eruptions where such deposits may make up a large proportion of distal ash (e.g. Dartevelle et al., 2002; Cashman and Rust, 2016; Engwell and Eychenne, 2016; Engwell et al., 2014; Eychenne et al., 2015; Eychenne et al., 2012; Rose and Durant, 2009). The goal of our work is to develop analytical tools to distinguish primary from secondary ash deposits.

Controlled laboratory experiments have provided some links between natural variables (e.g. degree of overpressure, transport distance) and the characteristics of the associated tephra deposit. Laboratory study of primary fragmentation is typically performed by shock-tube experimentation at magmatic temperatures. Results show that for a given sample porosity, greater degrees of overpressure increase the fragmentation efficiency and thus decrease the overall grain size (Kueppers et al., 2006b). Experimental GSDs typically follow power-law distributions with fractal dimensions (D) of ~2.5 (Kueppers et al., 2006a). Variations about this value are thought to reflect the energy of fragmentation, with higher fragmentation energies producing deposits with higher D values (Perugini and Kueppers, 2012). The fractal dimension increases by secondary fragmentation (Kaminski and Jaupart, 1998). The effects of secondary fragmentation have been quantified using experiments involving both collision and abrasion (Cagnoli and Manga, 2004; Mueller et al., 2015). Results confirm that the fine ash content increases with time, and that experiments involving abrasion produce finer ash than experiments involving impact (Mueller et al., 2015). Also important is the original clast density, with grain size reduction dominated by breakage of the more vesicular fragments (Kueppers et al., 2012). This observation has particular relevance to explosively generated ash, which often has TGSDs dictated by the vesicle size distribution (Genareau et al., 2012; Liu et al., 2015a; Rust and Cashman, 2011).

Less well studied is the role of crystals in fragmentation and ash formation. Crystals commonly form a major constituent of intermediate magmas; thus it seems likely that the abundance and size distributions of crystals would affect the size, density and shape of explosively generated fragments. In fact, crystal concentrations in ash deposits show that individual crystals typically have a limited size and density range (e.g., Martel et al., 2001; Cashman and Rust, 2016; Sparks and Walker, 1977). Crystals in ash fractions are often broken or rounded, possibly due to the fragmentation and/or ash generation mechanism (e.g. Bachmann et al., 2002; Best and Christiansen, 1997; Carter et al., 1986). The presence of broken crystals in explosive eruption deposits has previously been attributed to two main processes: melt inclusion (MI) decrepitation and shock fragmentation. Fragmentation by MI decrepitation occurs when overpressure in the MI exceeds the tensile strength of the crystal. This may

be achieved by cyclic periods of overheating linked to the latent heat of crystallisation (Bindeman, 2005; Zhang, 1998) or rapid decompression of crystal-bearing magma during ascent (Best and Christiansen, 1997; Bindeman, 2005; Miwa and Geshi, 2012; Tait, 1992; Williamson et al., 2010). Crystal fragmentation by shock fragmentation can occur by extensional fracture during decompression and subsequent melt vesiculation (Chouet et al., 1994; Kennedy et al., 2005; Miwa and Geshi, 2012; Pallister et al., 1996).

Here we present a multi-component analysis of experimentally fragmented pumice samples. Although the effects of both rapid decompression and abrasion have been previously investigated, we extend these experiments in several important ways. First, we focus on fragmentation of a vesicle- and crystal-rich intermediate magma by a range of methods. Second, we explore the effects of both primary and secondary fragmentation on the resulting shape, size and componentry of the particle population. Primary fragmentation is simulated by rapid decompression experiments in a shock tube while secondary processes (such as abrasion and impact in PDCs) are simulated in the laboratory by ball mill and falling piston experiments, respectively. Controlled experiments with the same starting material – pumice from recent eruptions of the Soufriere Hills Volcano (SHV) – allow us to compare the ash-generating efficiency of the different processes. Additionally, adding componentry analysis allows us to evaluate the extent to which (broken) crystals affect the grain size, shape and fractal dimension of the tephra deposit. Finally, we compare our experimental results with natural SHV ash samples from fallout deposits produced by a dome collapse and a Vulcanian eruption.

2. Methods

All experiments were conducted using a single crystalline andesite pumice block that survived decompression during an explosive (Vulcanian) eruption of SHV in February 2010. We fragmented the pumice sub-samples in three different ways: rapid decompression at both room temperature and 880˚C, impact and milling at room temperature - all within the brittle deformation field; (Alidibirov and Dingwell, 2000). To characterize the resulting material, we determined the total grain size distributions produced by each fragmentation method, as well as ash components, shapes and textures.

For the decompression experiments, we also compare crystal sizes and shapes before and after fragmentation.

2.1 Pre-fragmentation characterisation

The original sample had a dense-rock equivalent density of 2.69×10^3 kg m^{-3} and an estimated glass transition temperature (T_g) of ~790°C (Jones et al., 2013). For the decompression experiments we drilled four pumice cylinders, each measuring 60 mm long and ~25 mm in diameter. Prior to fragmentation the physical and textural properties were characterised. Crystal populations and pre-existing crystal fractures were quantified with X-Ray computed tomography (XRCT) and optical microscopy of thin sections; helium pycnometry was used to calculate connected and total porosities for the four samples (see Table 1).

2.1.1 X-Ray computed Tomography

Radiographs for XRCT were collected with a Nikon Meterology 225/320kV Custom Bay scanner located at the Henry Mosely X-Ray Imaging Facility, University of Manchester. Acquisition conditions were 41 kV accelerating voltage, 239 μA current and a 0.5 mm Al filter. An exposure time of 1000 ms was used for all scans. To reconstruct the scans, we first calculated the centre of rotation of all the radiographs and then applied a beam hardening correction using the Xtek CT Pro software.

All processing was conducted using the 3D visualization and segmentation software Avizo 8.0 Standard. Crystal volumes were determined from a sub-volume of ~ 2.5×10^8 voxels extracted from the raw image stack, where 1 voxel measures 0.02257 mm^3. A 3x3x3 voxel 3D median filter was applied to this sub-volume with three iterations. Each image in the stack was segmented and thresholded to identify phases based on their characteristic grey scale values. A binary data set was then created to generate either the surface or volume of the segmented crystals. Only objects of 5 voxels or larger were included in calculations of crystal volumes. The separation of pre-broken crystal fragments can be achieved when distances are > ~ 0.09 mm.

Mineral modes, porosity and bulk sample crystallinity were determined with a larger sub-volume of $6x10^8$ voxels, which required significantly more computational capacity than the crystal volume measurements, and therefore a different approach. Firstly a median filter was applied to the entire image stack with ImageJ software (http://rsbweb.nih.gov/ij/). Next pores and mafic and felsic mineral phases in each image were separated based on grey scale values with an ImageJ plugin, PhaseQuant (Elangovan et al., 2012). The small density variation between different mineral phases, and the corresponding similarity of grey scales, made segmentation of specific minerals difficult so crystals are classified as either mafic or felsic phases (e.g. Cnudde et al., 2006). Each segmented volume (felsic, mafic and pores) was then converted into a binary image stack and imported into Avizo. The felsic crystal data required a 3D erosion and subsequent dilation by two voxels to remove background noise. Finally, surface generation and volume analysis was performed.

2.1.2 Textural characterisation

A 3D rendered volume of an example sub-sampled volume (Figure 1a) shows the distribution of crystals prior to experimental fragmentation. Broken crystals are common, and often have a jigsaw-like fit. Where the separation between these crystal fragments was sufficient to resolve in the tomographic analysis, each crystal fragment was counted as a separate crystal. The average DRE crystallinity for crystals >32μm in diameter (5 φ) is 27 vol. % with ~21% felsic and ~6% mafic crystals and oxides. Point counts of petrographic thin sections of the same samples included smaller microlites, and thus yield a higher crystallinity (38%); this shows that about 11% of the total crystal volume is < 32 μm.

A crystal volume distribution (CVD) extracted from the rendered tomographic volumes is shown in Figure 1b. The crystals range in size from 10^{-5} to 10^{1} mm^3, with a mode of 10^{-3} mm^3. Measurement of broken crystals as individual fragments means that the rendered volume distribution accounts for pre-existing crystal breakage prior to experimental fragmentation, within the resolution of the imaging technique.

196

197 *2.3 Porosities and fragmentation threshold*

198 Porosity provides information about the potential energy available for fragmentation during
199 decompression (Kueppers et al., 2006b) and is used to calculate the minimum initial overpressure
200 required for complete fragmentation in the decompression experiments (Spieler et al., 2004). To
201 measure porosity, we cleaned the sample cores and measured their porosity by helium pycnometry,
202 using a Quantachrome Instruments Ultrapync 1200e pycnometer housed at LMU Munich, Germany.
203 Total porosity $\varnothing_T$ was calculated from the solid density ρ_s and the bulk sample density ρ as:

204 $$\varnothing_T = 1 - \frac{\rho}{\rho_s}, \qquad [1]$$

205 where ρ_s is the measured density of powdered sample milled to a grain size less than the minimum
206 pore size. The connected or open porosity $\varnothing_C$ is calculated as:

207 $$\varnothing_C = \left(\frac{V_C - V_M}{V_C}\right) \times 100\ , \quad [2]$$

208 where V_C is the geometrical volume of the cylindrical samples and V_M is the volume measured by He
209 pycnometry. The isolated (closed) porosity, $\varnothing_I$ can then be defined as:

210 $$\varnothing_I = \varnothing_T - \varnothing_C. \qquad [3]$$

211

212 The average total porosity is 66%, with a range of 1.25% between all sample cores. Individual
213 porosity values for the cores used in the four rapid decompression experiments are reported in Table
214 1.

215

216 *2.2 Experimental fragmentation*

217 Samples from the Soufriere Hills Volcano (SHV) were fragmented experimentally by three methods:
218 rapid decompression, hammer impacts and ball milling (Figure 2). Broadly, these aimed to replicate
219 three natural volcanic processes: magmatic overpressure and decompression, impact and abrasion/
220 milling in turbulent flow.

221 Rapid decompression-driven fragmentation was performed using a shock tube-like apparatus
222 (Figure 2a) at the LMU Munich, Germany (e.g. Scheu et al., 2008; Spieler et al., 2004). By using two

223 experimentally calibrated diaphragms we achieved a pressure differential of either 15 or 30 MPa; this
224 exceeds the fragmentation threshold by 12 and 27 MPa (Spieler et al., 2004). At each differential
225 pressure, experimental fragmentation was conducted at both 20˚C and 880ºC. The experimentally
226 generated pyroclasts were left to settle in the low pressure tank for 1-2 hours and then sieved to 125
227 μm using a pressure washer filled with distilled water. All material that passed through the 125 μm
228 sieve was left to settle for 2 days in a sediment collection tank.
229 Impact experiments were performed by placing a single rectangular block (~ 4 x 5 x 2cm) of
230 SHV pumice into a detachable steel cup, as illustrated in Figure 2b. A 10 kg steel piston was then
231 repeatedly dropped from a height of 50 cm. The fives experimental runs, each run with a different
232 block, comprised 5, 10, 15, 20 and 25 piston drops; at the end of each run the entire sample was
233 recovered from the basal cup by flushing with distilled water.
234 Ball mill grinding was performed using a Planetary Ball Mill PM 100 manufactured by
235 RETSCH Ltd. The initial GSD for the ball mill experiments, represented by "0 min" in Figure 3c, was
236 created by crushing ~ 10cm square blocks of SHV pumice. For each experiment an aliquot of this
237 input sample was weighed and placed into the agate jar of the ball mill (Figure 2c) along with six 1.6
238 cm diameter agate balls. The container was sealed and rotated at 450 rpm for 0.5, 1, 2.5 or 5 minutes,
239 and the sample removed for subsequent analysis.
240
241 *2.3 Post-fragmentation characterisation*
242 After fragmentation by the three methods (Figure 2) the experimental pyroclasts were
243 characterised by grain size, componentry, shape and fracture surface morphology.
244
245 *2.3.1 GSD measurements*
246 All particles coarser than 125 μm were separated into grain size fractions by manual sieving
247 into size bins of -3, -2, -1, 0, 1, 2, 3 phi (φ). Particle size analysis for material ≤ 250 μm was
248 performed at the Environmental Change Laboratory, University of Western England, Bristol, UK
249 using a Mastersizer 2000 laser diffraction particle size analyser, manufactured by Malvern

250 Instruments Ltd. Sieve and Mastersizer data were combined using the overlapping 3 φ size fraction to
251 produce a total grain size distribution for each fragmentation experiment.
252
253 *2.3.2 Componentry*
254 Componentry analysis was conducted under a binocular microscope for grain sizes -3 to 3 ϕ.
255 Grains ≥ 500 μm were picked manually; smaller grains were classified from analysis of digital
256 microscope images. Where possible, at least 300 grains were analysed for each grain size fraction.
257 Grains were separated into three component categories: (1) free mafic crystals, (2) free felsic crystals,
258 and (3) clasts (i.e. anything that is not a free crystal), where a free crystal is defined as having matrix
259 adhered to less than 20% of the surface of the crystal. Additional 2D componentry of the 2 φ ash
260 fraction was performed using backscattered electron (BSE) mode of Scanning Electron Microscopy
261 (SEM) on a Hitachi S-3500N SEM at the School of Earth Sciences, University of Bristol. This grain
262 size fraction was chosen for detailed analysis because all experiments produce sufficient samples of
263 this size fraction. Ash grains were set in resin and polished to expose grain interiors before being
264 carbon coated. A mosaic of 25 images was taken of each sample using BSE mode from a working
265 distance of 18 mm, a 15Kv accelerated voltage and a magnification of 60x. Each image had a 1024 x
266 768 pixel resolution. Componentry was performed manually by placing a grid on the image and
267 counting grains. Grains were subdivided into three components: (1) crystals with no attached matrix,
268 (2) crystals with matrix attached, and (3) vesicular matrix clasts (all matrix grains were vesicular).
269 The 3D morphology of fine ash samples was examined using secondary electron mode on the
270 SEM. Ash grains within the 2 φ sieve fraction were mounted on carbon-based stubs and Au coated to
271 a thickness of approximately 5 nm. For grains measuring 125-250 μm or 3 φ (the finest fraction
272 studied), silver paint was applied to the SEM stub prior to Au coating, to reduce the effects of
273 charging.
274
275 *3.2.3 Shape analysis*
276 The 2D SEM image mosaics of the 2 φ grain size fraction were analysed with ImageJ
277 software. Images of individual grains were thresholded and converted to binary format before

quantifying grain shapes using axial ratio and convexity. Only grains from the 'vesicular matrix' componentry category were analysed for shape as they displayed the most variation between sample runs. This component comprised between 10 and 60 % of the total depending on the fragmentation mechanism.

Axial ratio is the ratio of the axes of the particle's best-fit ellipse:

$$Axial\ Ratio\ (AR) = \frac{Minor\ Axis}{Major\ Axis}. \quad [4]$$

Convexity is defined as the ratio of the perimeter of the grain and its convex hull (the smallest convex polygon that contains the 2D shape):

$$Convexity = \frac{Perimeter\ of\ convex\ hull}{Perimeter}. \quad [5]$$

It is a measure of the surface roughness of the external shape boundary (Liu et al., 2015b), such that a high value of convexity indicates a smooth external surface.

Where a crystal comprised at least 10% of the entire grain, areas of crystals and matrix were also calculated separately by manually varying the greyscale threshold to generate separate binary images, then calculating the pixel area of each. Abrasion is expected to decrease the relative proportion of glassy matrix adhering to crystals. For this reason, Meyer (1971) define the "abrasion index", which is the ratio of the area of a crystal to the area of attached matrix. However, abrasion may not be the only process to affect the crystal-matrix ratio. Furthermore, Meyer's "abrasion index" is unbounded (i.e. becomes infinite if there is no matrix). For these reasons, we introduce a related parameter we call the Adherence Factor:

$$Adherence\ Factor\ (AF) = \frac{area\ of\ matrix}{area\ of\ matrix + area\ of\ crystal} \quad [6]$$

The adherence factor is bounded between one (matrix only with no dominant crystal) and zero (for a crystal with no adhered matrix) and therefore we expect AF to decrease with increasing abrasion.

4. Results

4.1 Grain size distributions

The grain size distributions (GSD) of all sample sets are limited to a maximum of -3φ because of initial sample size. Rapid decompression (Figure 3a) creates a sample suite with a median size of -2.30φ to 0.23φ. Most striking is the effect of changing fragmentation temperature, where elevated temperatures yield coarser GSDs. The grain size distributions produced from the falling piston experiments are notably more fine-grained than pyroclasts produced by rapid decompression. Median sizes range from 1.70φ to 5.03φ and generally decrease with increased number of hits (Figure 3b). The grain size resulting from 10 hits, however, is abnormally small relative to the other data sets; we attribute this to natural heterogeneity within the pumice block that was the source of the starting material of each experiment. Experimentally generated pyroclasts from ball milling show a systematic increase in fine particles with increased milling duration. All GSDs produced by milling show a pronounced fine tail and are skewed to smaller sizes than GSDs from the rapid decompression and falling piston experiments.

4.2 Ash shape

Vesicular grains (i.e. all those that were not dominated by a single large crystal of over 10% of the total grain) were analysed for two shape parameters: axial ratio and convexity. Axial ratio is a representation of particle elongation, while convexity quantifies the smoothness of the grain exterior (Liu et al., 2015b). Axial ratio values vary considerably depending on the experimental fragmentation method (Figure 4a-c). Ash produced by rapid decompression has a greater range of axial ratio values than those produced by milling or impact. Ash grains from the milling experiments showed the smallest range of axial ratios although the range increased with milling time: axial ratios of grains milled for 1 minute have a lower mode and extend to larger values than axial ratios of grains milled for 0.5 minutes (Figure 4c). In contrast, axial ratio values changed little with number of impacts (Figure 4b). However, convexity data show that increased impacts smoothed out the irregular grain surfaces in the comparative grain size fraction: the ash grains produced by 10 piston impacts have greater average convexity values, and thus less irregular exteriors, than grains produced by 5 impacts (Figure 4e).

329

330 *4.3 Experimentally generated pyroclast componentry*

331 Componentry analysis of the pyroclasts generated by rapid-decompression required the proportions of
332 free mafic and felsic crystals (those with < 20% adhered matrix) to be discriminated from other matrix
333 dominated clasts (Figure 5a). No free crystals were observed at grain sizes greater than -1 φ. At finer
334 grain sizes the proportion of crystals varies considerably for different grain size fractions. Within
335 these coarse-grained rapid decompression products, free crystals (mainly felsic) are most abundant in
336 the 1φ size fraction, contributing ~40 weight % to this grain size bin. The maximum abundance of
337 mafic crystals varies between 1 and 2 φ for different experimental runs. We observed no systematic
338 componentry changes in the decompression experiments (Fig. 5a) as a function of either ΔP or
339 fragmentation temperature; the small variations between experimental runs likely relate to slight
340 sample heterogeneities prior to experimental fragmentation.

341

342 Within the 2φ fraction (Fig. 5b), there are only small differences in SEM componentry between the
343 hot and cold rapid decompression products. Both have similar proportion of free crystals (with no
344 attached matrix) although there is a higher proportion of crystals with attached matrix in the products
345 of hot decompression (Figure 5b). More dramatic is the comparison with data from other
346 fragmentation mechanisms, where products of the milling and impact experiments show a higher
347 proportion of free crystals than the decompression products. Additionally, the sample milled for
348 longer (1 min) has a higher proportion of free crystals than its counterpart that was milled for 30
349 seconds. A similar trend is observed in the impact products: the sample that underwent 10 hits has a
350 greater proportion of free crystals than the sample that was hit five times. These observations show
351 that repeated fragmentation removes crystal coatings and frees individual crystals from the matrix.

352

353 *4.4 Crystal volume distributions*

354 The crystal populations within the original SHV pumice cores and the pyroclasts produced by rapid
355 decompression were quantified by analysis of X-Ray CT (Figure 1) and SEM analysis (Figure 5a),
356 respectively. To effectively compare these pre-experiment and post-experiment crystal populations,

357 the crystal volume distributions generated by X-Ray-CT were converted to a length scale. We assume
358 that all crystals within the volcanic rock samples form euhedral cuboid volumes,

359 $$V_{xal} = h \times w \times l \qquad [7]$$

360 where *h* and *w* represent the height and width of the smallest crystal face and *l* is length. Assuming
361 that crystals have aspect ratios of 2:1 and that the minor and intermediate axes are the restrictive
362 dimensions of the sieve size (*d*), an effective particle diameter is calculated as:

363 $$d = \left(\frac{V_{xal}}{2}\right)^{1/3} \qquad [8]$$

364 Effective diameters are converted to the φ scale, the volumes falling in each φ bin summed and
365 converted to weight % to form the "Rock" data set in Figure 6.
366
367 The crystal population generated by decompression is determined by averaging the mass of
368 mafic/felsic crystals within each size fraction of all decompression experiments. We average because
369 no significant difference in componentry was observed when changing fragmentation overpressure or
370 temperature. These data are then converted to weight % of total crystals and form the "Ash" data set
371 in Figure 6.
372
373 The size distribution of crystals within the ash relative to those in the SHV pumice (Figure 6) shows
374 that rapid decompression caused the crystal size to decrease. Grain size reduction is concentrated
375 over the central portion of the size range investigated. In coarser grain size fractions (2 - 0 φ) the
376 crystal abundance in the pumice is greater than the abundance in the ash and is dominated by felsic
377 crystals. Conversely, in the finer fractions (1 - 3 φ) crystals are more abundant in the ash than in the
378 original pumice. Moreover, there are no crystals within the -2φ ash fraction, although they were
379 present in the pumice prior to decompression and fragmentation. This suggests that crystals were not
380 simply freed from the matrix during fragmentation but were also reduced in size by crystal breakage.
381
382 *4.5 SEM imagery of fracture surfaces*

383 Photomicrographs of the 2φ ash fraction produced by rapid decompression reveal characteristics of
384 broken crystal surfaces (Figure 7) that can be classified as: (1) smooth, clean surfaces with negligible
385 topographic relief (Figure 7a) and (2) rougher, often highly irregular surfaces displaying intense river-
386 line fracturing and hackles (Figures 7c and 7d). On some crystals, a vesicular glass coating is
387 observed (Figure 7b); it is slightly more common in the hot fragmentation experiments relative to the
388 room temperature runs. No other differences were observed in the fracture surfaces or styles between
389 the products of hot and cold experiments. About 90% of broken crystals have clean broken surfaces
390 with negligible topographic relief. We interpret these as breakage along a cleavage plane or a pre-
391 existing internal fracture (Figure 7a). Where river-line fractures are observed on these surfaces they
392 are widely spaced and have low relief. Only about 10% of broken crystal surfaces are much rougher
393 and complex due to fractures cross-cutting cleavage planes (e.g. Figure 7d).
394
395 Finally, sub-circular cavities, including some with protruding glass strands, are a rare but ubiquitous
396 feature of crystal surfaces in the experimental products. Similar features were observed by
397 Williamson et al. (2010) in natural SHV pumice and interpreted as melt inclusions that burst within a
398 plastic groundmass due to a major decompression event (e.g. dome collapse). Melt extension is a
399 non-brittle process that could not have been generated through experimental fragmentation at room
400 temperature. The fact that we observe these features in the experiment products indicates that they
401 must already have existed in the dome/pumice samples prior to decompression in the laboratory.
402
403 **5. Discussion**
404 We have explored several techniques to characterise both experimentally generated ash and its parent
405 material (Table 1). We now use these results - from grain size measurements, fractal analysis,
406 componentry and shape descriptors - to examine the effects of different fragmentation mechanisms on
407 pyroclast characteristics. For samples that were rapidly decompressed, we couple this analysis with
408 XRCT and SE SEM imagery to examine how rapid decompression-driven fragmentation alters the
409 crystal population. Lastly, to illustrate our techniques we compare experimentally generated SHV ash
410 to two natural SHV ash examples.

411

412 *5.1 Fractal behaviour of products*

413 Since the idea of fractal behaviour was introduced to Earth Sciences (e.g., Korvin, 1992; Turcotte,
414 1986), power law exponents (fractal dimension D values) have been used to quantify the size
415 distributions of volcanic pyroclastic products (e.g., Kaminski and Jaupart, 1998; Perugini et al., 2011;
416 Taddeucci et al., 2004). Higher power law exponents represent tephra deposits that are dominated by
417 finer ash fractions. Therefore fractal dimensions are commonly used to infer the fragmentation
418 efficiency and have been linked to the energy available for fragmentation (e.g., Kueppers et al.,
419 2006a).

420

421 It has long been noted that tephra produced from volcanic eruptions commonly has a much higher
422 fractal dimension (larger fine ash component) than expected from simple crushing or rock
423 disaggregation (Hartmann, 1969). The source of this fine ash is an open question, but is clearly
424 dictated ultimately by the vesicle size distribution (Rust and Cashman, 2011). Kaminski and Jaupart
425 (1998) proposed a model of secondary fragmentation based on experimental fragmentation, where
426 they assumed that piston impact causes primary fragmentation while grinding in a ball-mill caused
427 secondary fragmentation. In this scenario, primary fragmentation initially creates $D=2.5\pm0.1$, then
428 ongoing selective re-fragmentation through particle-particle collisions increases the values of $D \geq 3$
429 preserved in fall deposits. However, many experimental fragmentation experiments fail to replicate
430 the high power law exponents observed in natural pyroclastic deposits (Table 2). This leads to a
431 question about the mechanism(s) capable of producing the finer ash, particularly the role of the
432 original bubble population in controlling the final grain size distribution (Rust and Cashman, 2011).

433

434 We analysed the fractal dimension of the total GSD for all experimental fragmentation methods by
435 converting raw data (mass proportion of particles in different size bins; Figure 3) to number-based
436 data to aid comparison to other published data sets (e.g. Kueppers et al., 2006a). Over the size range
437 analysed here, all experimentally produced ash samples follow a power law distribution, that is, they
438 plot on a straight line in log(N)–log(L) space (Figure 8), where N represents the number of grains

439 larger than corresponding fragment size (L) and the slope defines the fractal dimension (D). The
440 power-law distributions were fitted to the total GSD recovered from the experiments. In some cases
441 one or two data points are excluded at the coarse or fine tail (open circles in Figure S1).
442
443 The log(N) vs. log(L) data for the rapid decompression experiments (Figure 8a) form linear trends
444 with fractal dimensions between 2.03 and 2.24, in good agreement with other studies that have used
445 the same fragmentation method (Kueppers et al., 2006a; Kueppers et al., 2006b; Perugini and
446 Kueppers, 2012). Pyroclasts from the impact (falling piston) experiments also show a fractal
447 distribution (Figure 8b) with a mean D = 2.60. This value is comparable to values from simple
448 crushing and disaggregation of rocks (Table 2; Hartman, 1969). The falling piston sample set shows
449 the most variation. Here D values do not vary systematically with number of impacts, although the
450 power law exponents do broadly increase with increased number of impacts. In these analyses, we
451 excluded the tails of the fragment size distribution when calculating D (represented as open circles in
452 Figure S1), which may account for minor disparities. The milling experiments follow a power law
453 distribution, which shows a systematic increase in D from 2.33 at 0.5 min to 2.45 at 5 mins (Figure
454 8c). This progressive rise in D suggests that milling not only creates fine ash but also causes the fine
455 ash component to become increasingly dominant in the TGSD.
456
457 Our experimental data show that secondary fragmentation can progressively increase D from an initial
458 value resembling rapid decompression-driven fragmentation to higher values. Yet, even after
459 considerable milling durations (5mins) or a large number (25) of successive impacts, the experimental
460 products do not exceed D values of 3. Furthermore, analysis of the 2φ fraction shows that the crystals
461 were not being broken through milling, rather they were being stripped of adhering groundmass. This
462 suggests that during secondary fragmentation of crystal rich tephra, the crystal population may help to
463 sustain a relatively coarse control on the GSD. This interpretation is supported by data from eruptions
464 of Heimaey, Fuego and Oshima, where the basaltic pyroclasts are rich in microphenocrysts and the
465 TGSDs have fractal dimensions D~1.9-2.3. Silicic deposits (Mount St. Helens, El Chichon and
466 Quizapu), in contrast, have both low (or no) groundmass crystallinity and D values >3 (Table 2).

Assuming all of the eruptions listed in Table 2 involved secondary, as well as primary, fragmentation (through both milling and impacts, either with the conduit wall or within the particle-rich plume at depth), the differences in observed D seem most easily explained by variations in groundmass crystallinity. Where large proportions of crystals are present in the starting magma they provide a coarse control on the grain size distribution and prevent production of high proportions of fine ash; this keeps D values low (< 3). The 'final' D value is therefore a function of both magma and fragmentation characteristics, including magma porosity and permeability, magma crystallinity, fragmentation overpressure and the degree of mechanical processing.

5.2 Fragmentation control on pyroclast characteristics

Our analysis confirms results from previous experimental studies, including the effect of mechanical fragmentation in shifting the GSD to smaller sizes (Cagnoli and Manga, 2004; Kueppers et al., 2012; Mueller et al., 2015) and the high efficiency of abrasion relative to impact experiments in producing fine ash (Mueller et al., 2015; Figure 3). We also found that the proportion of vesicular fragments decreased with increased milling time and number of impacts (Figure 5b), consistent with Kueppers et al. (2012).

Our experiments also show that the mechanism of fragmentation has a significant effect on the characteristics of individual pyroclasts. Of particular note is the variation in the axial ratios of matrix fragments between the three fragmentation mechanisms studied (Figure 4). The axial ratios of impact and milling products are large compared to the decompression products, which suggests that increased mechanical abrasion prevents, or rapidly reduces, the likelihood of producing elongated fragments. Additional milling further increases the mean and range of axial ratio values of ash particles. This is interesting because the small ash particles mimic shape variations previously observed in larger pumice clasts, both in rock tumbling experiments and natural PDC deposits (e.g., Manga et al., 2011). Studies of pumice clast rounding further suggest that both rounding and ash production via comminution are most efficient proximal to volcanic vents, where PDCs are most energetic.

493 A sizeable portion of the experimental products includes crystals with adhered matrix (Fig. 5b). Past
494 studies have used these fragments as a marker for the amount of abrasion (Freundt and Schmincke,
495 1992; Meyer, 1971). We quantified this effect using an 'Adherence Factor' (AF: Equation 6; Figure
496 9). Our data show that the decompression experiments have a substantially higher AF (more adhered
497 matrix) than the products of impact and milling. Hot decompression causes particles to retain slightly
498 more matrix material than cold decompression. Interestingly, increasing the number of impacts or
499 time of milling does not appear to dramatically alter the AF, but the products of milling have a lower
500 AF, overall, than the products of impact.

501 To interpret the mechanisms responsible for adhered matrix produced by different fragmentation
502 methods, it is also important to consider the effect of crystal breakage on AF. We identified broken
503 crystals by recording whether the crystal displayed at least one intact ring of zoning or whether the
504 zoning was interrupted. In the products of rapid decompression, the crystals with a lower AF value
505 were typically broken. However, there is no obvious correlation between crystal breakage and AF in
506 the products of milling and impacts (Figure S2); this lack of correlation may be due to these two
507 mechanisms not dramatically increasing the number of broken crystals. As a consequence, the matrix
508 is stripped from the outside without breaking the crystal, resulting in many whole crystals with a low
509 AF value. In contrast, the low AF of broken crystals within products of rapid decompression suggests
510 that, as crystals break, internal crystal surfaces are exposed and the area of adhered matrix decreases.
511 Therefore we suggest crystal breakage is the main mechanism for reducing AF during rapid
512 decompression.

513

514 *5.3 The influence of crystals on fragmentation during rapid decompression*

515 Crystals commonly form a major constituent of erupting magmas and there is the potential for the
516 abundance and size distributions of crystals to affect the size, density and shape of fragments
517 generated in explosive eruptions. The componentry analysis presented here demonstrates that free
518 crystals contribute a significant mass (up to 40%) to specific grain size fractions produced by rapid
519 decompression (Figure 5a). The size range in which crystals dominate appears independent of

fragmentation pressure and temperature and is directly related to the crystal size distribution in the starting material. Over the grain size range studied (-3 to 3 φ), plagioclase dominates the total crystal population within each size fraction of the experimentally generated fragments. This agrees with modal analysis of the starting material that showed it to be the most abundant mineral. As illustrated in Figure 5a, free crystals are non-existent or of trivial abundance in the grain size fractions coarser than 0 φ, consistent with the initial crystal size population in the starting material (Rock curve in Fig.6). The mafic crystals show a broader peak at smaller grain sizes, which is likely related to the initial size populations. Therefore the textural characteristics of the starting volcanic material (magma analogue) directly control the experimentally produced tephra (PDC analogue).

High proportions of crystals within a grain size fraction have the potential to alter the bulk ash density, especially at coarser grain sizes. This, in turn, will cause differential settling of crystals relative to glass fragments of similar size, particularly if the glass is vesicular (e.g., Sparks and Walker, 1977). This effect has been documented in natural eruptive products of Mount St Helens and Quizapu (Cashman and Rust, 2016), where the proportion of free crystals decreases faster with distance from the vent than pumice or glass shards from the same eruption. Currently, ash dispersion models (e.g. Tephra 2; Bonadonna et al., 2010) commonly use a single vesicular glass ash density to represent all grain size fractions from a volcanic eruption. Improvements could therefore be made to more accurately represent crystal-rich pyroclasts, particularly in eruptions characterised by PDCs.

Crystal size distributions may also help to explain the production of crystal pyroclasts devoid of glass coatings. If a whole (micro)phenocryst were to be extracted from the fragmenting magma, the surface would likely be at least partially coated in a glass. However, if internal broken fragments of a once larger phenocryst are extracted, then the relative chance of a glass-coated surface is low. Knowing the surface properties of ash has implications for remote sensing applications and surface leachate studies. Our componentry study suggests that free crystals in the ash generated by rapid decompression represent broken fragments from once larger whole crystals; this is likely because during rapid

547 decompression fragmentation, the crystals cannot accommodate deformation and hence fracture
548 (Cordonnier et al., 2009).
549
550 Crystal fracture topographies indicate that breaking of crystals in our decompression experiments was
551 dominantly along cleavage surfaces (type 1 fractures) with only about 10% of fractures cross-cutting
552 cleavage planes (Figure 7). Crystals tend to break or 'cleave' along a particular crystallographic
553 orientation because cleavage planes have a relatively low surface energy (Hull, 1999; Kelly and
554 Macmillan, 1986). Experimental studies and natural observations of plagioclase identify intra-
555 crystalline fractures controlled by crystallography and preferential fracture along cleavage planes (e.g.
556 Borg and Heard, 1970; Brown and Macaudiére, 1984). Further, Kennedy et al. (2005) use fractures in
557 SHV hornblende crystals to infer the orientation of tensile unloading and therefore the shape of the
558 fragmentation front. Under mode I tensile failure, cleavage surfaces have a direct and primary effect
559 on fragmentation behaviour. When cleavage planes are orientated perpendicular to the tensile force
560 (parallel to the unloading wave) then simple cleavage fracture is expected to occur (e.g., Figure 7a).
561 However, when cleavage planes are orientated obliquely to tensile forces, then mode II failure can aid
562 fracture by the formation of shear couples (Figure 7c). Therefore, the orientation angle, defined as the
563 angle between the cleavage plane and the tensile force vector, will influence the relative proportions
564 of mode I and II failure.
565
566 *5.4 Comparison with natural samples*
567 To compare with our experimental results, we also studied two ash samples from fallout deposits
568 produced by a dome collapse event (on 31 March 1997) and a Vulcanian eruption (on 26 September
569 1997) of Soufriere Hills Volcano. The dome collapse event generated PDCs but no plume at the vent,
570 making the fallout deposit entirely co-PDC in origin (Bonadonna et al., 2002; Engwell and Eychenne,
571 2016). The Vulcanian eruption produced both an eruptive column at the vent and PDCs on the
572 volcano's flank; the fallout deposit consequently includes ash from both vent-derived and co-PDC
573 plumes (Bonadonna et al., 2002). These two natural events, with distinct eruption characteristics,
574 allow us to demonstrate how our analysis techniques can be used on natural material to identify

575 secondary fragmentation. To compare with experimental samples, we analysed the componentry, AF
576 (Figure 9) and proportion of broken crystals in the 2 φ grain size fraction (Figure S2) of each sample.

577 The 2 φ fraction of both natural samples comprises approximately 30% dense material (crystals,
578 phenocrysts and vesicle-free glass). The Vulcanian sample however, contains 15% crystals with
579 adhered glass whereas the dome collapse sample contains approximately 20% (Figure 10). Hence the
580 Vulcanian sample comprises approximately 55% vesicular fragments, while the ash produced by
581 dome collapse contains less than 50%. Of this vesicular portion, the Vulcanian sample is comprised
582 mostly of microlite-free vesicular glass fragments. In comparison, the dome collapse sample is
583 comprised entirely of the microlite-rich vesicular glass. The higher proportion of vesicular microlite-
584 free glass in the Vulcanian sample indicates that in addition to microlite-bearing magma stored at
585 shallow levels (top of the conduit or dome), deep magma was erupted in the Vulcanian explosion. In
586 contrast, the dome collapse event involved only material previously extruded in the dome, comprising
587 microlite-rich glass of variable vesicularity. The two natural samples also differ in patterns of matrix
588 adherence. The AF distribution of the Vulcanian sample is trimodal, with a major mode at AF ~0.2
589 (low adhering matrix) and two minor modes at AF ~0.6 and 0.8 (Figs. 9 and S2). In comparison, the
590 dome collapse sample shows a uniform AF distribution (Figure 9) and a higher proportion of broken
591 crystals at low AF values (Figure S2).

592 Although this natural case study is illustrative only, and uses a single grain size fraction at a single
593 location for each eruption, both the components and the AF distributions are distinctive. The
594 differences in componentry (vesicle and microlite content) of the natural samples can be explained by
595 the fact that they experienced different ascent and fragmentation histories and different transportation
596 modes (PDCs vs. plumes); both of which should affect the mechanical properties. The Vulcanian
597 sample includes both particles transported directly in a plume and particles that were first transported
598 in PDCs before being entrained into co-PDC plumes. These two events can be observed, respectively,
599 in Figure 9 as a group of poorly abraded particles (high AF values) and a set of highly abraded
600 particles (low AF values). The dome collapse sample is dominated by microlite-rich particles that
601 were entirely transported in PDCs. The uniform AF distribution suggests that abrasion during

602 transport did not affect all the phenocrysts uniformly. Differences might reflect: (1) the robustness of
603 particles due to their high microlite content and moderate vesicularity compared to the highly
604 vesicular, microlite-free particles produced by the Vulcanian eruption; and/or (2) the coarser initial
605 grain size distribution in the dome collapse block-and-ash flows compared to the explosively
606 produced Vulcanian pumice flows, whereby larger initial particle sizes would require more abrasion
607 to release phenocrysts from the matrix. This points to a limitation of our analysis, which is that we
608 have not attempted to assess variations as a function of time/distance. At Tungurahua volcano, it has
609 been suggested that dense crystal-rich PDCs become increasingly crystal rich with time/distance as
610 the vesicular material is removed through abrasion (Douillet et al., 2013). This hypothesis could be
611 tested by applying our techniques to an appropriate selection of samples from a range of locations.

612

613 **6. Conclusions**

614 Three fragmentation methods (rapid decompression, impact and milling) have been explored to
615 constrain fragmentation associated with three different eruptive processes (Figure 11). Analysed
616 GSDs are fractal, which means that they can be characterised by the fractal dimension D. Our data
617 show that an initial GSD with $D \approx 2.1$ produced by rapid decompression can be altered by secondary
618 fragmentation processes that generate fine particles. Importantly, however, D values produced by
619 secondary processes in our experiments reach only ~2.7 (Fig. 8), which is far from $D > 3$ observed in
620 many silicic eruptions (e.g., Kaminski and Jaupart, 1998; Rust and Cashman, 2011). We suggest that
621 the relatively low D values reflect the role of the groundmass crystal population, which prevents
622 extensive crushing and grain size reduction.

623

624 We support this hypothesis by analysis of particle shape (Fig. 4), componentry (Fig. 5) and adherence
625 factor (AF; Fig. 9). These data show that secondary fragmentation by either impact or milling
626 dramatically reduces the matrix component (Fig. 5b); ash generated by milling becomes increasingly
627 rounded (less elongate), and ash exteriors generated by impacts becomes increasingly smooth (Fig. 4).
628 Both milling and impact also remove adhering matrix from crystals (decrease AF), with milling the

most efficient at this process. Importantly, products of primary fragmentation retain much more adhering matrix than products of secondary fragmentation by either milling or impact (Fig. 9). Together these data provide guidelines for assessing primary vs. secondary contributions to the total grain size population within an eruptive deposit.

To further explore the role of crystals, we analysed the crystal content of volcanic ash derived from rapid decompression. Most crystals fracture along cleavage planes, leaving a smooth and clean breakage surface. During the evacuation of a crystal-rich magma body driven by rapid decompression, crystal fragmentation is inevitable and indeed characteristic of the associated tephra fallout. The proportion of free crystals depends on the grain size considered. X-Ray CT measurements combined with componentry allowed us to describe the shift in crystal size during fragmentation by rapid decompression. These data are important because the size fractions dominated by juvenile crystals show enhanced sedimentation because crystal densities exceed those of vesicular clasts. Thus we suggest that consideration of crystal sizes and proportions could improve settling calculations that inform hazard maps and dispersion models.

Finally we illustrate the application of our analysis techniques to two samples from Soufriere Hills Volcano, Montserrat: one dome collapse sample with co-PDC ash only, and one Vulcanian sample with contributions from both primary and co-PDC fragmentation. These samples are distinct in both their components and their grain characteristics, particularly AF. The Vulcanian sample is dominated by deep-derived microlite-poor and highly vesicular glass. Ash particles have polymodal AF distributions, with a dominant mode at low AF (little adhering glass) and two other modes at higher AF. We suggest that the high AF modes reflect primary fragmentation, while the low AF mode is the signature of co-PDC ash. The dome collapse sample, in contrast, is dominated by microlite-rich glass of variable vesicularity. In this sample, the AF distribution is approximately uniform, and most likely reflects the wide range of groundmass textures (both vesicularity and crystallinity). This latter observation brings up one further point, which is that both primary and secondary fragmentation processes are strongly dependent on the original magma components. As a result, a full understanding

of ash attributes produced by different mechanisms requires a systematic study using starting materials with different bubble and crystal attributes.

Acknowledgements

We thank the Henry Mosely X-Ray Imaging Facility, University of Manchester for their support with the XRCT. Klaus Mayer and Cristian Montanaro are thanked for their support with the shock tube experiments. KVC acknowledges the support of the AXA Research Fund and a Royal Society Research Merit Award. TJJ was partly supported by NERC studentship NE/L0025901.

References:

Alatorre-Ibargüengoitia, M. A., Scheu, B., Dingwell, D. B., Delgado-Granados, H., and Taddeucci, J., 2010, Energy consumption by magmatic fragmentation and pyroclast ejection during Vulcanian eruptions: Earth and Planetary Science Letters, v. 291, no. 1, p. 60-69.

Alfano, F., Bonadonna, C., Volentik, A. C., Connor, C. B., Watt, S. F., Pyle, D. M., and Connor, L. J., 2011, Tephra stratigraphy and eruptive volume of the May, 2008, Chaitén eruption, Chile: Bulletin of Volcanology, v. 73, no. 5, p. 613-630.

Alidibirov, M., and Dingwell, D. B., 2000, Three fragmentation mechanisms for highly viscous magma under rapid decompression: Journal of Volcanology and Geothermal Research, v. 100, no. 1–4, p. 413-421.

Bachmann, O., Dungan, M. A., and Lipman, P. W., 2002, The Fish Canyon magma body, San Juan volcanic field, Colorado: rejuvenation and eruption of an upper-crustal batholith: Journal of Petrology, v. 43, no. 8, p. 1469-1503.

Best, M. G., and Christiansen, E. H., 1997, Origin of broken phenocrysts in ash-flow tuffs: Geological Society of America Bulletin, v. 109, no. 1, p. 63-73.

Bindeman, I. N., 2005, Fragmentation phenomena in populations of magmatic crystals: American Mineralogist, v. 90, no. 11-12, p. 1801-1815.

Bonadonna, C., Connor, L. J., Connor, C. B., and Courtland, L. M., 2010, Tephra2.

Bonadonna, C., Mayberry, G., Calder, E., Sparks, R., Choux, C., Jackson, P., Lejeune, A., Loughlin, S., Norton, G., and Rose, W., 2002, Tephra fallout in the eruption of Soufrière Hills Volcano, Montserrat: Geological Society, London, Memoirs, v. 21, no. 1, p. 483-516.

Borg, I. Y., and Heard, H. C., 1970, Experimental Deformation Of Plagioclases, *in* Paulitsch, P., ed., Experimental and Natural Rock Deformation / Experimentelle und natürliche Gesteinsverformung, Springer Berlin Heidelberg, p. 375-403.

Brown, W. L., and Macaudiére, J., 1984, Microfracturing in relation to atomic structure of plagioclase from a deformed meta-anorthosite: Journal of Structural Geology, v. 6, no. 5, p. 579-586.

Cagnoli, B., and Manga, M., 2004, Granular mass flows and Coulomb's friction in shear cell experiments: Implications for geophysical flows: Journal of Geophysical Research: Earth Surface (2003–2012), v. 109, no. F4.

Carter, N. L., Officer, C. B., Chesner, C. A., and Rose, W. I., 1986, Dynamic deformation of volcanic ejecta from the Toba caldera: Possible relevance to Cretaceous/Tertiary boundary phenomena: Geology, v. 14, no. 5, p. 380-383.

Chouet, B. A., Page, R. A., Stephens, C. D., Lahr, J. C., and Power, J. A., 1994, Precursory swarms of long-period events at Redoubt Volcano (1989–1990), Alaska: Their origin and use as a forecasting tool: Journal of Volcanology and Geothermal Research, v. 62, no. 1–4, p. 95-135.

Cnudde, V., Masschaele, B., Dierick, M., Vlassenbroeck, J., Hoorebeke, L. V., and Jacobs, P., 2006, Recent progress in X-ray CT as a geosciences tool: Applied Geochemistry, v. 21, no. 5, p. 826-832.

Cordonnier, B., Hess, K. U., Lavallee, Y., and Dingwell, D. B., 2009, Rheological properties of dome lavas: Case study of Unzen volcano: Earth and Planetary Science Letters, v. 279, no. 3–4, p. 263-272.

Dartevelle, S., Ernst, G. G., Stix, J., and Bernard, A., 2002, Origin of the Mount Pinatubo climactic eruption cloud: Implications for volcanic hazards and atmospheric impacts: Geology, v. 30, no. 7, p. 663-666.

Douillet, G. A., Tsang-Hin-Sun, È., Kueppers, U., Letort, J., Pacheco, D. A., Goldstein, F., Von Aulock, F., Lavallée, Y., Hanson, J. B., and Bustillos, J., 2013, Sedimentology and geomorphology of the deposits from the August 2006 pyroclastic density currents at Tungurahua volcano, Ecuador: Bulletin of Volcanology, v. 75, no. 11, p. 1-21.

Dufek, J., and Manga, M., 2008, In situ production of ash in pyroclastic flows: Journal of Geophysical Research: Solid Earth, v. 113, no. B9.

Elangovan, P., Hezel, D. C., Howard, L., Armstrong, R., and Abel, R. L., 2012, PhaseQuant: A tool for quantifying tomographic data sets of geological specimens: Computers & Geosciences, v. 48, no. 0, p. 323-329.

Engwell, S., Sparks, R., and Carey, S., 2014, Physical characteristics of tephra layers in the deep sea realm: the Campanian Ignimbrite eruption: Geological Society, London, Special Publications, v. 398, no. 1, p. 47-64.

Engwell, S., **Eychenne, J.**, **2016.** Chapter 4: Contribution of fine ash to the atmosphere from plumes associated with pyroclastic density currents. In *Volcanic Ash: Hazard Observation*, edited by Mackie, S., Ricketts, H., Watson, M., Cashman, K., Rust, A. *Elsevier. 67-85pp.*

Eychenne, J., Cashman, K., Rust, A., and Durant, A., 2015, Impact of the lateral blast on the spatial pattern and grain size characteristics of the 18 May 1980 Mount St. Helens fallout deposit: Journal of Geophysical Research: Solid Earth, v. 120, no. 9, p. 6018-6038.

Eychenne, J., Le Pennec, J.-L., Troncoso, L., Gouhier, M., and Nedelec, J.-M., 2012, Causes and consequences of bimodal grain-size distribution of tephra fall deposited during the August 2006 Tungurahua eruption (Ecuador): Bulletin of volcanology, v. 74, no. 1, p. 187-205.

Félix, G., and Thomas, N., 2004, Relation between dry granular flow regimes and morphology of deposits: formation of levées in pyroclastic deposits: Earth and Planetary Science Letters, v. 221, no. 1, p. 197-213.

Freundt, A., and Schmincke, H.-U., 1992, Abrasion in pyroclastic flows: Geologische Rundschau, v. 81, no. 2, p. 383-389.

Genareau, K., Proussevitch, A. A., Durant, A. J., Mulukutla, G., and Sahagian, D. L., 2012, Sizing up the bubbles that produce very fine ash during explosive volcanic eruptions: Geophysical Research Letters, v. 39, no. 15.

Hartmann, W. K., 1969, Terrestrial, lunar, and interplanetary rock fragmentation: Icarus, v. 10, no. 2, p. 201-213.

Hull, D., 1999, Fractography: observing, measuring and interpreting fracture surface topography, Cambridge University Press.

Jones, T., Wadsworth, F., Vasseur, J., Lavallee, Y., Hess, K., Scheu, B., and Dingwell, D., Porosity and Textural Evolution of Bubbly Magma under High-Temperature Uniaxial Deformation, *in* Proceedings AGU Fall Meeting Abstracts2013, Volume 1, p. 2715.

Kaminski, E., and Jaupart, C., 1998, The size distribution of pyroclasts and the fragmentation sequence in explosive volcanic eruptions: Journal of Geophysical Research: Solid Earth, v. 103, no. B12, p. 29759-29779.

751 Kelly, A., and Macmillan, N. H., 1986, Strong solids, Clarendon Press Oxford.
752 Kennedy, B., Spieler, O., Scheu, B., Kueppers, U., Taddeucci, J., and Dingwell, D. B., 2005, Conduit
753 implosion during Vulcanian eruptions: Geology, v. 33, no. 7, p. 581-584.
754 Korvin, G., 1992, Fractal models in the earth sciences, Elsevier Science Ltd.
755 Kueppers, U., Perugini, D., and Dingwell, D. B., 2006a, "Explosive energy" during volcanic eruptions
756 from fractal analysis of pyroclasts: Earth and Planetary Science Letters, v. 248, no. 3, p. 800-
757 807.
758 Kueppers, U., Putz, C., Spieler, O., and Dingwell, D. B., 2012, Abrasion in pyroclastic density currents:
759 insights from tumbling experiments: Physics and Chemistry of the Earth, Parts A/B/C, v. 45,
760 p. 33-39.
761 Kueppers, U., Scheu, B., Spieler, O., and Dingwell, D. B., 2006b, Fragmentation efficiency of explosive
762 volcanic eruptions: a study of experimentally generated pyroclasts: Journal of Volcanology
763 and Geothermal Research, v. 153, no. 1, p. 125-135.
764 Liu, E., Cashman, K., Rust, A., and Gislason, S., 2015a, The role of bubbles in generating fine ash
765 during hydromagmatic eruptions: Geology, v. 43, no. 3, p. 239-242.
766 Liu, E. J., Cashman, K. V., and Rust, A. C., 2015b, Optimising shape analysis to quantify volcanic ash
767 morphology: GeoResJ, v. 8, p. 14-30.
768 Manga, M., Patel, A., and Dufek, J., 2011, Rounding of pumice clasts during transport: field
769 measurements and laboratory studies: Bulletin of Volcanology, v. 73, no. 3, p. 321-333.
770 Martel, C., Dingwell, D. B., Spieler, O., Pichavant, M., and Wilke, M., 2001, Experimental
771 fragmentation of crystal-and vesicle-bearing silicic melts: Bulletin of volcanology, v. 63, no. 6,
772 p. 398-405.
773 Meyer, J., 1971, Glass crust on intratelluric phenocrysts in volcanic ash as a measure of eruptive
774 violence: Bulletin Volcanologique, v. 35, no. 2, p. 358-368.
775 Miwa, T., and Geshi, N., 2012, Decompression rate of magma at fragmentation: Inference from
776 broken crystals in pumice of vulcanian eruption: Journal of Volcanology and Geothermal
777 Research, v. 227, p. 76-84.
778 Mueller, S. B., Lane, S. J., and Kueppers, U., 2015, Lab-scale ash production by abrasion and collision
779 experiments of porous volcanic samples: Journal of Volcanology and Geothermal Research,
780 v. 302, p. 163-172.
781 Pallister, J. S., Hoblitt, R. P., Meeker, G. P., Knight, R. J., and Siems, D. F., 1996, Magma mixing at
782 Mount Pinatubo: petrographic and chemical evidence from the 1991 deposits: Fire and Mud:
783 Eruptions and Lahars of Mount Pinatubo, Philippines. Quezon City: Philippine Institute of
784 Volcanology and Seismology, p. 687-731.
785 Perugini, D., and Kueppers, U., 2012, Fractal analysis of experimentally generated pyroclasts: A tool
786 for volcanic hazard assessment: Acta Geophysica, v. 60, no. 3, p. 682-698.
787 Perugini, D., Speziali, A., Caricchi, L., and Kueppers, U., 2011, Application of fractal fragmentation
788 theory to natural pyroclastic deposits: Insights into volcanic explosivity of the Valentano
789 scoria cone (Italy): Journal of Volcanology and Geothermal Research, v. 202, no. 3, p. 200-
790 210.
791 Rose, W., and Durant, A., 2009, Fine ash content of explosive eruptions: Journal of Volcanology and
792 Geothermal Research, v. 186, no. 1, p. 32-39.
793 Rust, A., and Cashman, K., 2011, Permeability controls on expansion and size distributions of
794 pyroclasts: Journal of Geophysical Research: Solid Earth, v. 116, no. B11.
795 Scheu, B., Kueppers, U., Mueller, S., Spieler, O., and Dingwell, D. B., 2008, Experimental volcanology
796 on eruptive products of Unzen volcano: Journal of Volcanology and Geothermal Research, v.
797 175, no. 1–2, p. 110-119.
798 Sparks, R., and Walker, G., 1977, The significance of vitric-enriched air-fall ashes associated with
799 crystal-enriched ignimbrites: Journal of Volcanology and Geothermal Research, v. 2, no. 4, p.
800 329-341.

801 Spieler, O., Kennedy, B., Kueppers, U., Dingwell, D. B., Scheu, B., and Taddeucci, J., 2004, The
802 fragmentation threshold of pyroclastic rocks: Earth and Planetary Science Letters, v. 226, no.
803 1–2, p. 139-148.
804 Taddeucci, J., Pompilio, M., and Scarlato, P., 2004, Conduit processes during the July–August 2001
805 explosive activity of Mt. Etna (Italy): inferences from glass chemistry and crystal size
806 distribution of ash particles: Journal of Volcanology and Geothermal Research, v. 137, no. 1,
807 p. 33-54.
808 Tait, S., 1992, Selective preservation of melt inclusions in igneous phenocrysts: American
809 Mineralogist, v. 77, no. 1-2, p. 146-155.
810 Turcotte, D., 1986, Fractals and fragmentation: Journal of Geophysical Research: Solid Earth (1978–
811 2012), v. 91, no. B2, p. 1921-1926.
812 Walker, G. P., 1973, Explosive volcanic eruptions—a new classification scheme: Geologische
813 Rundschau, v. 62, no. 2, p. 431-446.
814 Williamson, B., Di Muro, A., Horwell, C., Spieler, O., and Llewellin, E., 2010, Injection of vesicular
815 magma into an andesitic dome at the effusive–explosive transition: Earth and Planetary
816 Science Letters, v. 295, no. 1, p. 83-90.
817 Zhang, Y., 1998, Mechanical and phase equilibria in inclusion-host systems: Earth and Planetary
818 Science Letters, v. 157, no. 3-4, p. 209-222.
819 Zimanowski, B., Wohletz, K., Dellino, P., and Büttner, R., 2003, The volcanic ash problem: Journal of
820 Volcanology and Geothermal Research, v. 122, no. 1, p. 1-5.

821

822 **Figure Captions:**

823

824 **Figure 1:** 3D surface reconstructions of the crystal phases. Processed using Avizo software from X-
825 Ray computed tomography generated image stacks. **(a)** SHV subvolume. **(b)** Cumulative frequency
826 diagram showing the relative crystal volume distributions within SHV pumice extracted from 3D
827 reconstructions.

828

829 **Figure 2:** Diagrams of the various fragmentation apparatus used in this study. **(a)** shock tube
830 (modified after Alatorre-Ibargüengoitia et al. (2010)) , **(b)** falling piston and **(c)** ball mill.

831

832 **Figure 3:** Grain size distributions for **(a)** rapid decompression shock tube, **(b)** falling piston and **(c)**
833 ball mill experiments.

834

835 **Figure 4:** Shape analysis from BSE SEM images of 2φ grain size fraction. Histograms show shape
836 data gathered from 2D SEM image mosaics. Where an axial ratio of one implies a perfectly round
837 grain and a convexity of one implies a smooth grain with the same perimeter as its convex hull. **(a)**
838 The difference in axial ratio of the grains produced by hot and cold decompression. **(b)** The change in
839 the axial ratio value for grains that were hit 5 and 10 times. **(c)** The change in the axial ratio value for
840 grains that were milled for 30 seconds and one minute. **(d)** The difference in convexity values of the
841 grains produced by hot and cold decompression. **(e)** The change in value of convexity in grains hit 5
842 and 10 times. **(f)** The change in the value of convexity for grains that were milled for 30 seconds and
843 one minute.

844

845 **Figure 5:** Componentry results for experimentally generated ash. **(a)** SHV average componentry
846 results from rapid decompression, normalised per grain size fraction. **(b)** Individual ash grain
847 componentry from the 2φ grain size fraction using BSE SEM images of products of varying
848 fragmentation techniques.

849

Figure 6: Normalised crystal distributions for SHV represented as a cumulative distribution. Solid lines represent the crystal population present in the volcanic core prior to experimental fragmentation. Dashed lines represent the experimentally fragmented crystal population.

Figure 7: SEM micrographs of crystals from the SHV 2φ ash fraction. **(a)** Hornblende crystal showing mainly a clean flat surface however extremely irregular at the edges. **(b)** Broken crystal with a thin vesicular glass coating. **(c)** Hornblende crystal with a stepped fracture surface. **(d)** A plagioclase crystal showing multiple river line fractures on broken crystal surface.

Figure 8: Power law plots for **(a)** the rapid decompression experiments, **(b)** the falling piston experiments and **(c)** the ball mill experiments. Data markers represent those included in the linear regression.

Figure 9: Adherence Factor plot of the three fragmentation techniques: Milling (0.5 minutes and 1 minute), Impact (5 hits and 10 hits) rapid decompression (cold and hot) and natural samples (Vulcanian and dome collapse). Adherence Factor (AF) = area of matrix / (area of matrix + area of crystal) against the total cumulative per cent. A high value for AF represents a higher proportion of adhered matrix and thus the upper curve shows a greater amount of 'matrix stripping' than the lower curve. Normalised Grain No. is the value of AF in descending order, normalised to one.

Figure 10: Componentry of two natural SHV samples. The samples are from fallout deposits produced by a dome collapse event (on 31 March 1997) and a Vulcanian eruption (on 26 September 1997) of Soufriere Hills Volcano.

Figure 11: A summary cartoon relating the three experimental fragmentation mechanism to the natural volcanic scenario. Primary fragmentation through rapid decompression produces pyroclasts

with D ~2.2. Then through abrasion and milling, selective secondary fragmentation increases D and adds to the fine ash component to the GSD.

Table 1: Summary of all experimental runs and characterisation. Grey fields indicate that the characterisation has been performed.

Table 2: A review of relevant fragmented material and the associated fractal dimensions obtained.

Figure S1: Individual power-law plots for each experimental fragmentation experiment: **(a)** rapid decompression **(b)** impact and **(c)** milling. Open circles represent the data points not included in the linear fitting.

Figure S2: Histogram of adherence factor values for decompression (hot and cold), impact (5 hits and 10 hits), milling (30 seconds and 1 minute) and natural samples (Vulcanian and dome collapse). Shown on bars is the proportion of broken crystals amongst the crystal population where a broken crystal is defined as a crystal that clearly does not display an intact ring of zoning.

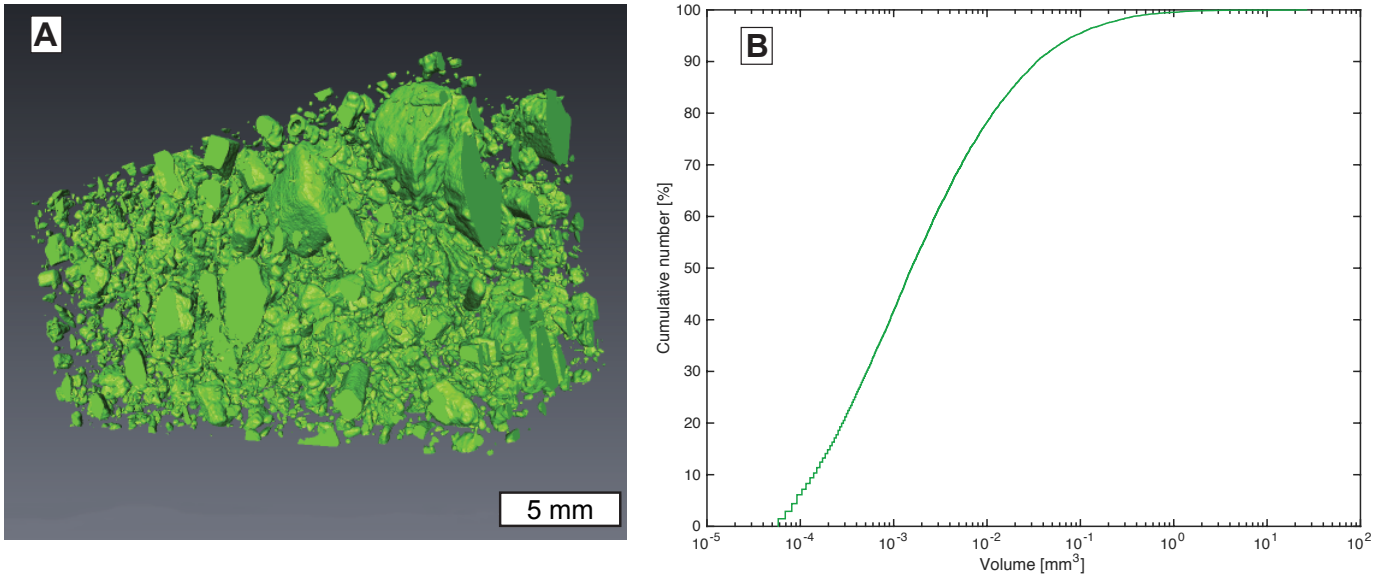

Figure 1: Jones et al (2016, JVGR)
Size: 1.5 column

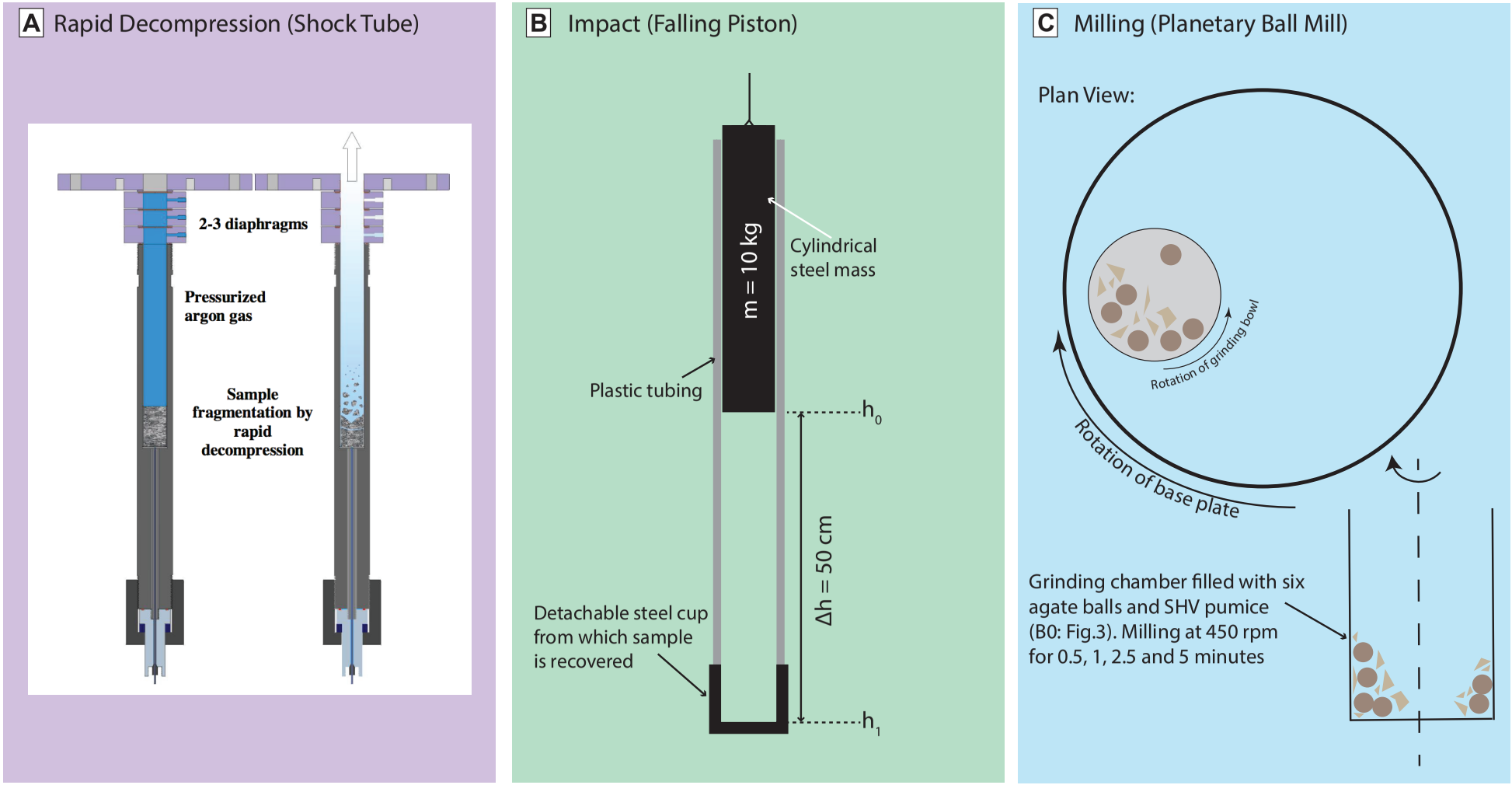

Figure 2: Jones et al. (2016, JVGR)
Size: Double column

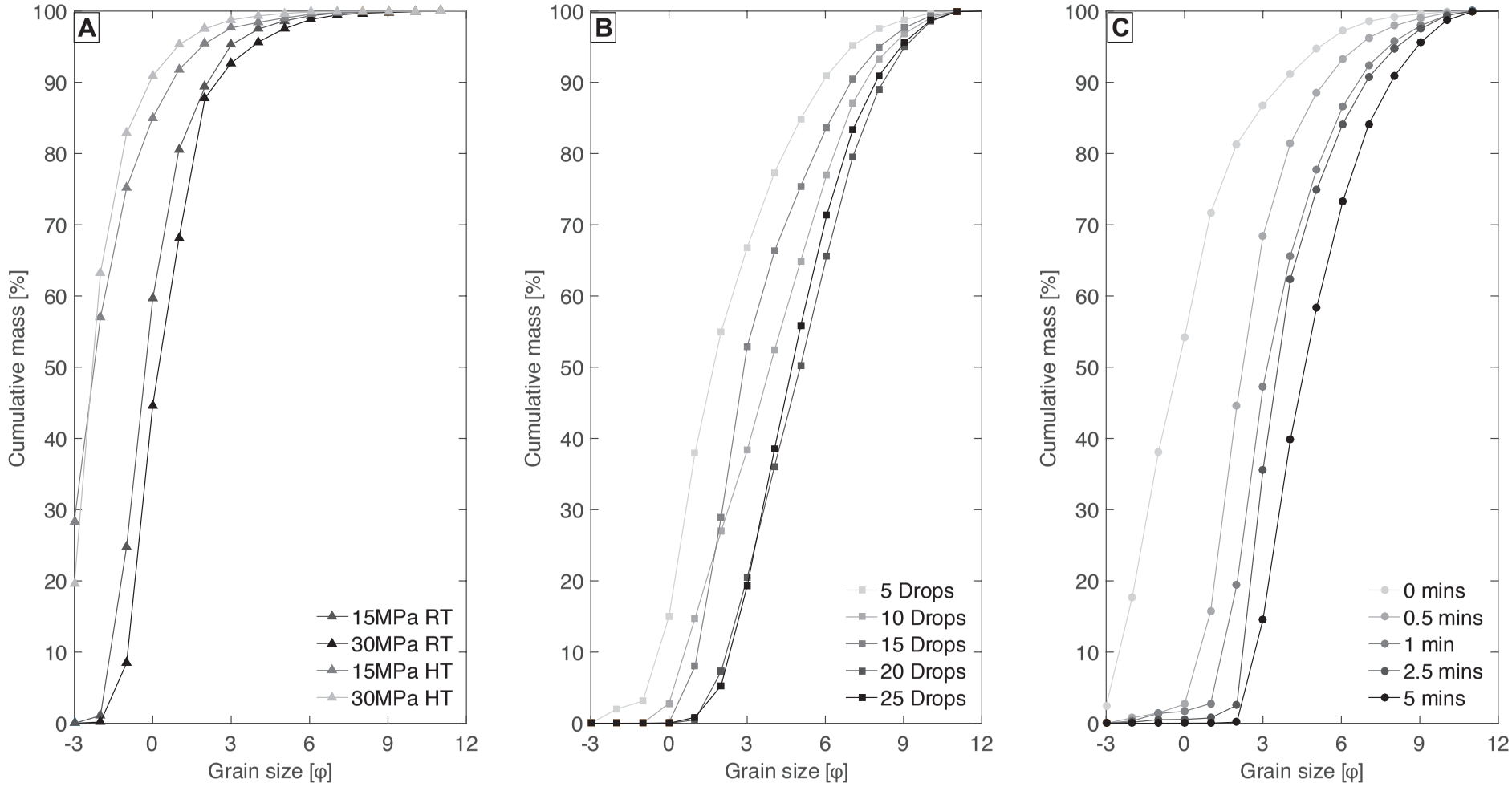

Figure 3: Jones et al. (2016, JVGR)
Size: Double column

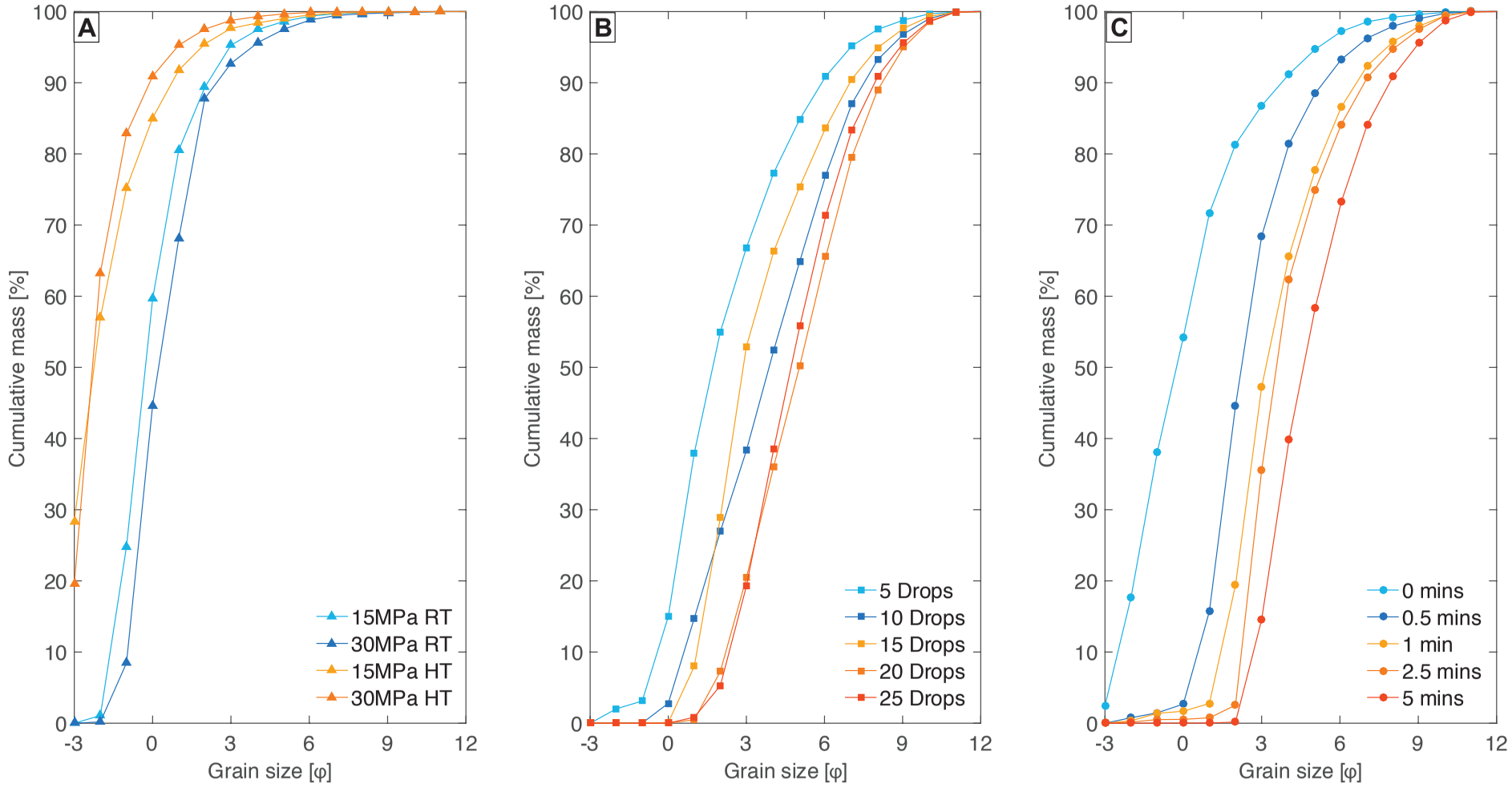

Figure 3: Jones et al. (2016, JVGR)
Size: Double column

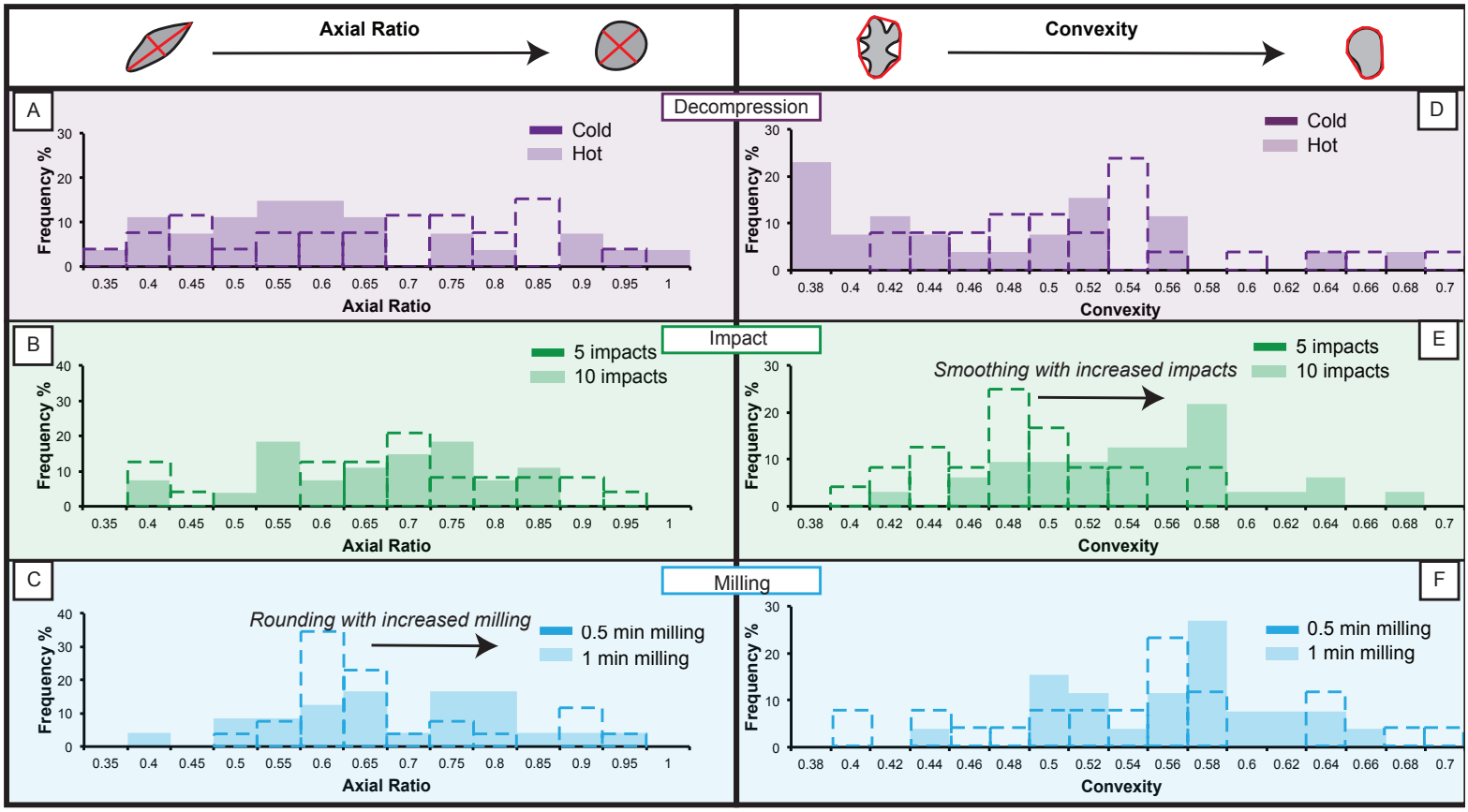

Figure 4: Jones et al. (2016, JGVR)
Size: 2 column

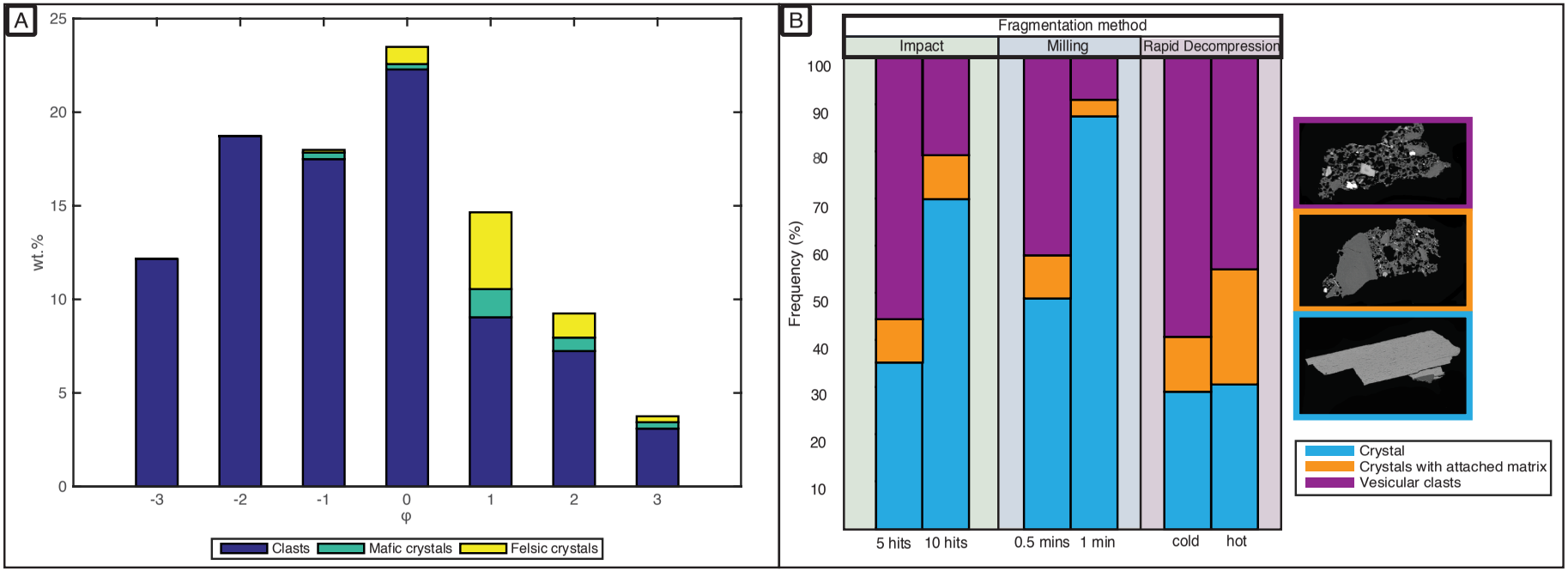

Figure 5: Jones et al (2016, JVGR)
Size: Double Collumn

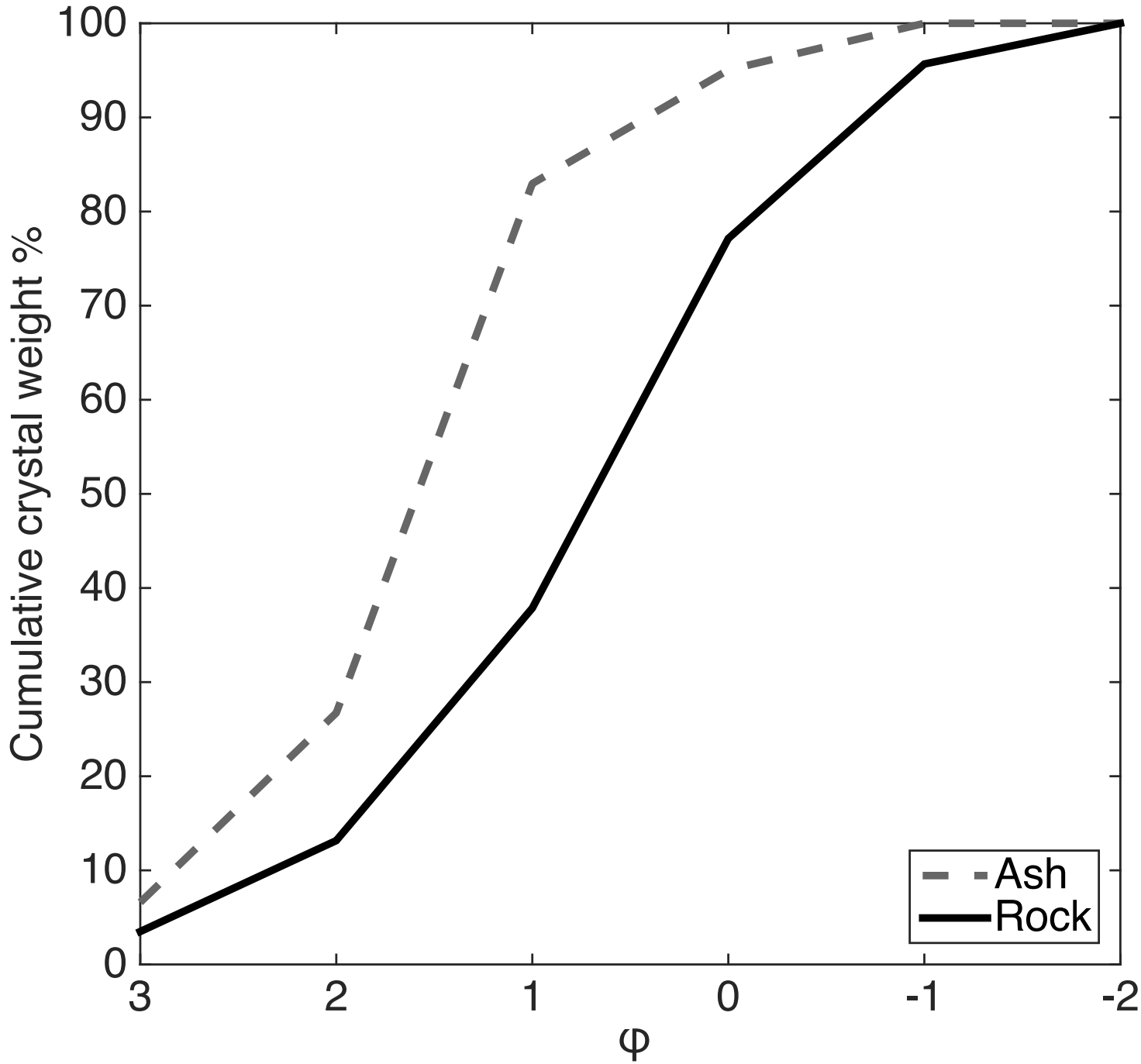

Figure 6: Jones et al. (2016, JVGR) Size: Single Column

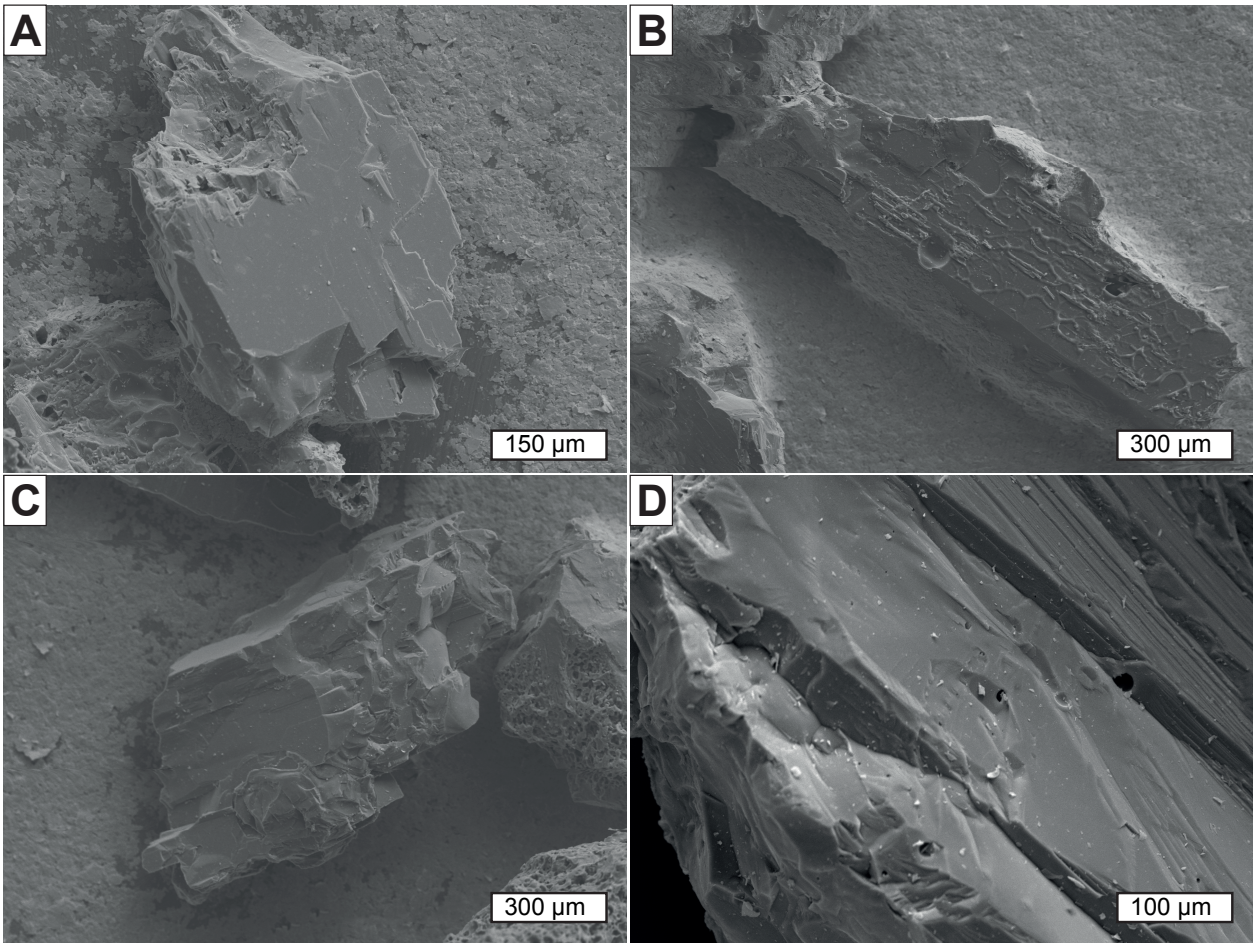

Figure 7: Jones et al (2016, JVGR)
Size: Single column

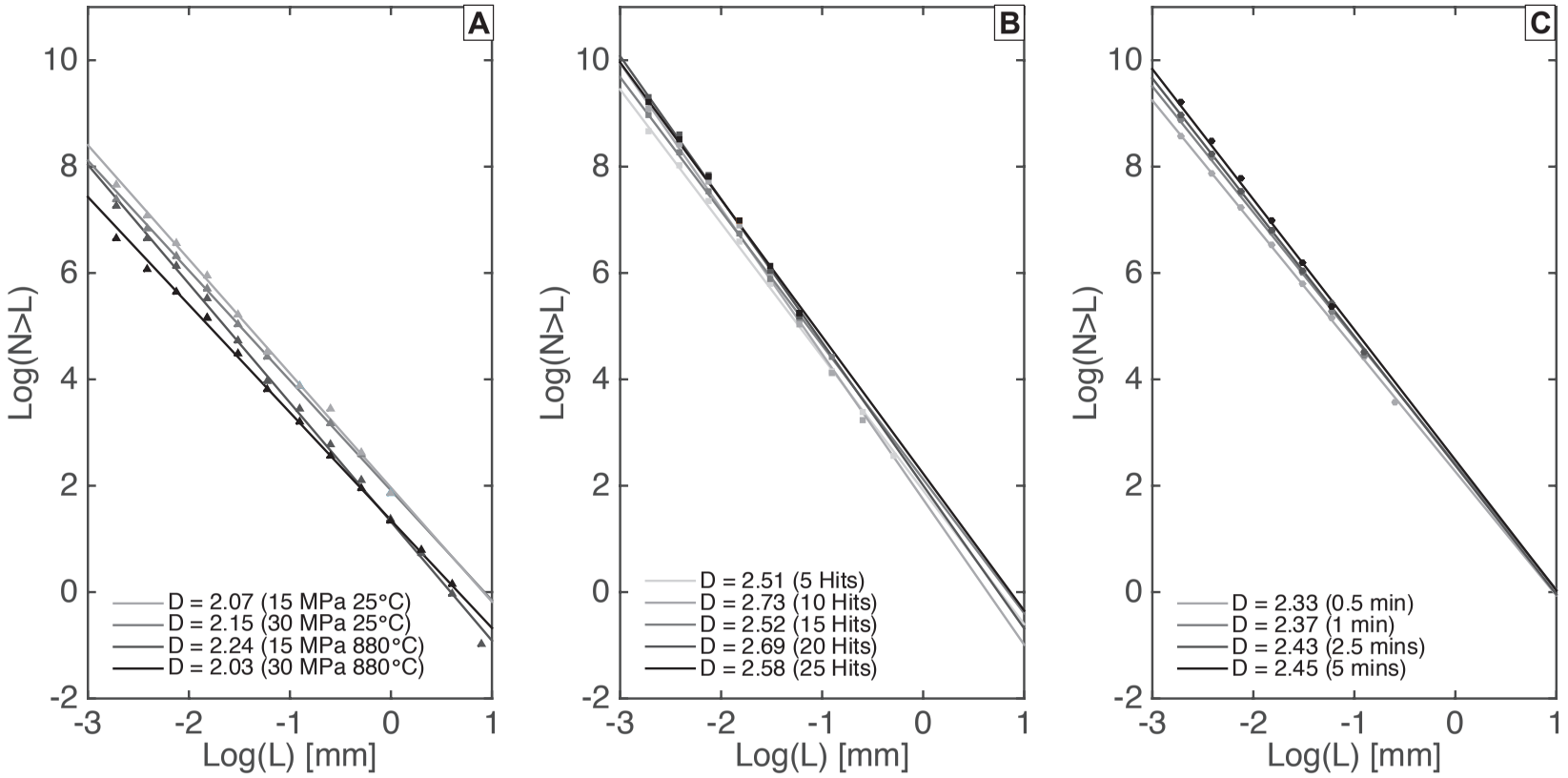

Figure 8: Jones et al. (2016, JVGR)
Size: Double column

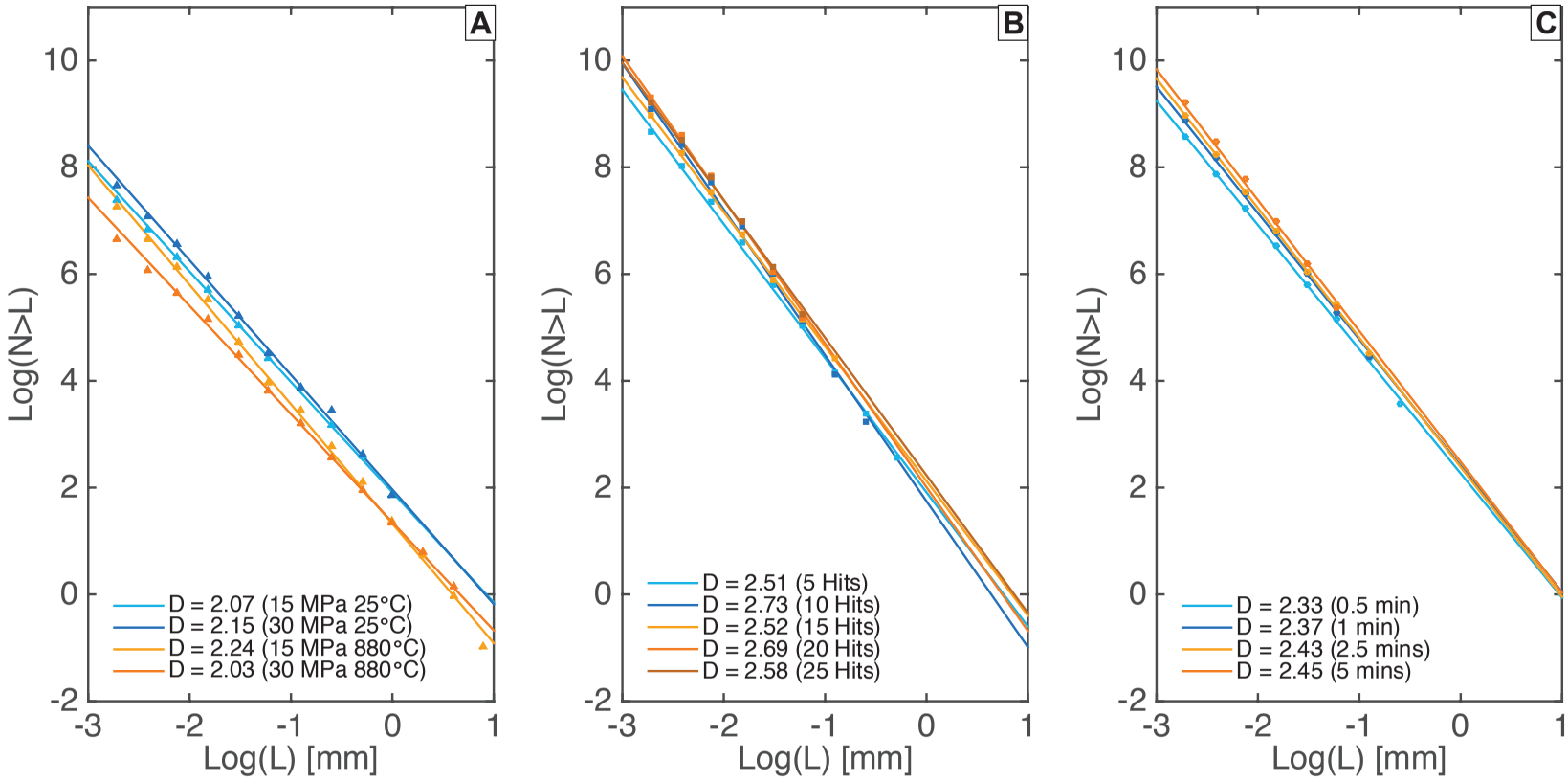

Figure 8: Jones et al. (2016, JVGR)
Size: Double column

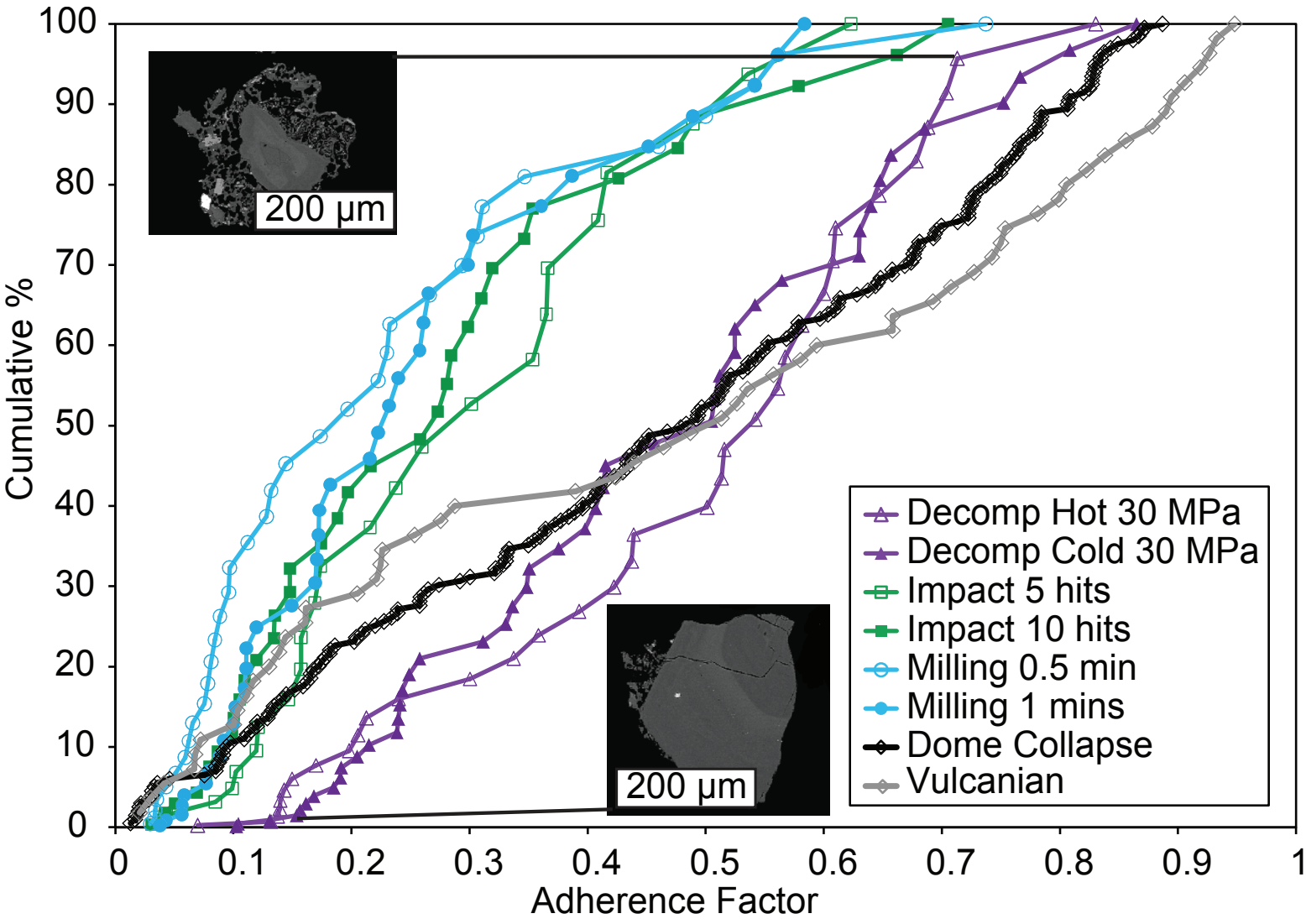

Figure 9: Jones et al. (2016, JGVR)
Size: Single column

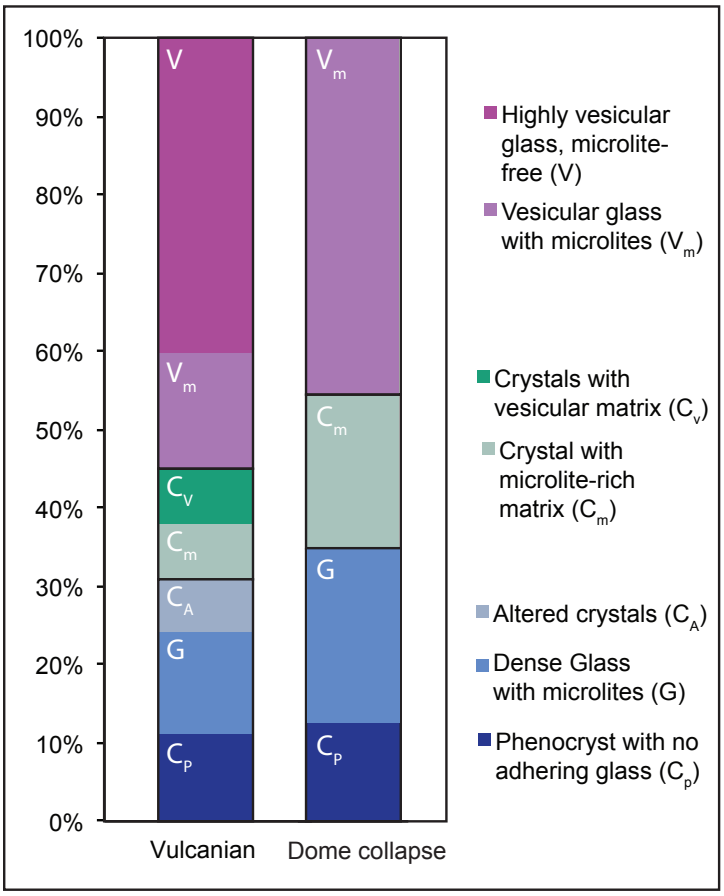

Figure 10: Jones et al. (2016, JVGR)
Size: Single Column

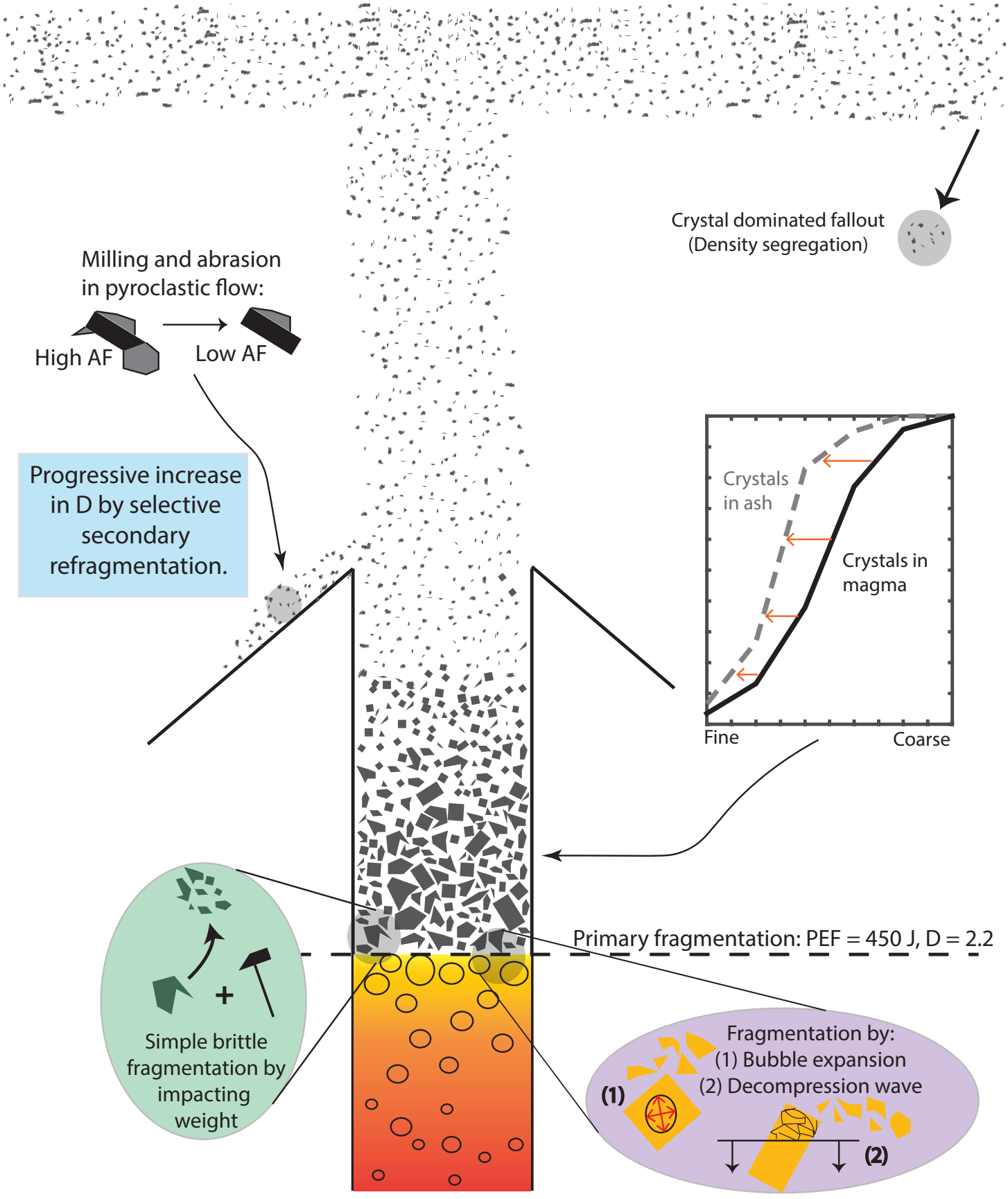

Figure 11: Jones et al (2016, JVGR)
Size: Single collumn